Large Eddy Simulation of Impinging Jets with Heat Transfer

by

Thomas Hällqvist

March 2006
Technical Reports from
Royal Institute of Technology
Department of Mechanics
S-100 44 Stockholm, Sweden

Akademisk avhandling som med tillstånd av Kungliga Tekniska Högskolan i Stockholm framlägges till offentlig granskning för avläggande av teknologie doktorsexamen fredagen den 3 Mars 2006 kl 10.15 i sal F3, Kungliga Tekniska Högskolan, Lindstedtsvägen 26, Stockholm.

Universitetsservice US-AB, Stockholm 2006

Thomas Hällqvist 2006, **Large Eddy Simulation of Impinging Jets with Heat Transfer**

KTH Mechanics, SE-100 44 Stockholm, Sweden

Abstract

This thesis deals with Large Eddy Simulation (LES) of impinging air jets. The impinging jet configuration features heated circular jets impinging onto a flat plate. The problem addressed here is of generic nature, with applications in many engineering devices, such as cooling of components in gas turbines, in cars and electronic devices. The flow is inherently unsteady and contains relatively slowly varying coherent structures. Therefore, LES is the method of choice when the Reynolds number is large enough to exclude Direct Numerical Simulations (DNS).

The present LES model is a basic model without explicit Sub-Grid-Scale (SGS) modeling and without explicit filtering. Instead, the numerical scheme is used to account for the necessary amount of dissipation. By using the computational grid as a filter the cutoff wavenumber depends explicitly on the grid spacing. The underlying computational grid is staggered and constructed in a Cartesian coordinate system. Heat transfer is modeled by the transport equation for a passive scalar. This is possible due to the negligible influence of buoyancy which implies constant density throughout the flow field. The present method provides accurate results for simple geometries in an efficient manner.

A great variety of inlet conditions have been considered in order to elucidate how the dynamics of the flow and heat transfer are affected. The considered studies include top-hat and mollified mean velocity profiles subjected to random and sinusoidal perturbations and top-hat profiles superimposed with solid body rotation. It has been found that the shape of the mean inlet velocity profile has a decisive influence on the development of the flow and scalar fields, whereas the characteristics of the imposed artificial disturbances (under consideration) have somewhat weaker effect. In order to obtain results unequivocally comparable to experimental data on turbulent impinging jets both space and time correlations of the inflow data must be considered, so also the spectral content. This is particularly important if the region of interest is close to the velocity inlet, i.e. for small nozzle-to-plate spacings. Within this work mainly small nozzle-to-plate spacings are considered (within the range of 0.25 and 4 nozzle diameters), which emphasizes the importance of the inflow conditions. Thus, additional to the basic methods also turbulent inflow conditions, acquired from a precursor pipe simulation, have been examined. Both for swirling and non-swirling flows. This method emulates fully developed turbulent pipe flow conditions and is the best in the sense of being well defined, but it demands a great deal of computing power and is also rather inflexibility. In case of the basic randomly perturbed

methods the top-hat approach has been found to produce results in closest agreement with those originating from turbulent inlet conditions.

In the present simulations the growth of individual instability modes is clearly detected. The character of the instability is strongly influenced by the imposed boundary conditions. Due to the lack of correlation random superimposed fluctuations have only a weak influence on the developing flow field. The shape of the mean profile, on the other hand, influences both the growth rate and the frequency of the dominant modes. The top-hat profile yields a higher natural frequency than the mollified. Furthermore, for the top-hat profile coalescence of pairs of vortices takes place within the shear-layer of the axial jet, whereas for the mollified profile (for the considered degree of mollification) it takes place within the wall jet. This indicates that the transition process is delayed for smoother profiles.

The amount of wall heat transfer is directly influenced by the character of the convective vortical structures. For the mollified cases wall heat transfer originates predominantly from the dynamics of discrete coherent structures. The influence from eddy structures is low and hence Reynolds analogy is applicable, at least in regions of attached flow. The top-hat and the turbulent inflow conditions yield a higher rate of incoherent small scale structures. This strongly affects the character of wall heat transfer. Also the applied level of swirl at the velocity inlet has significant influence on the rate of heat transfer. The turbulence level increases with swirl, which is positive for heat transfer, and so also the spreading of the jet. The latter effect has a negative influence on wall heat transfer, particularly in the center most regions. This however depends also on the details of the inflow data.

Descriptors: Impinging jet, large eddy simulation, heat transfer, vortex formation, circular jet, forcing, inflow conditions, implicit modeling.

Contents

Part I

Overview and summary

CHAPTER 1

Introduction

Within the truck manufacturing industry there is continuous development of the vehicle performance. The consequence of this is, among other things, engines with higher and higher output power. During the last 20 years there has been a monotone increase of the engine power. In the early eighties the most powerful truck engines had about 400 bhp. Today they have almost 700 bhp. This progress is dictated by the market and it is anticipated that it will continue in a similar manner also in the future. One of the consequences of this progress, combined with the need for compactness, is tougher demands on the cooling performance. To reach these demands one may consider larger and optimized radiators, higher fan speed, aerodynamic optimization of the engine compartment and of the front grill. On a truck these modifications are costly and challenging to implement.

Parallel to the progress of increasing engine power is the decrease of free space in the engine compartment. This originates from, among other things, lower cab floor and bulky noise and heat insulation. There is also an increasing number of components mounted on the engine or within the engine compartment, such as electronic and mechanical devices. These components are often sensitive to heat and require additional heat insulation. They may also represent additional heat generating sources, such as EGR (Exhaust Gas Recirculation) and retarders (hydrodynamic breaking system) that make the cooling of the engine, and surrounding components, even more challenging.

The two above described trends drastically increase the demands for efficient cooling. As the limitations are severe all possible improvements contribute to a step in the right direction. The work presented in this thesis represents a phase in a project aimed at improving the engine cooling capacity of Scania heavy trucks. This is performed by studying a basic impinging jet geometry with sophisticated analyzing and modeling methods. In this way the origin of heat transfer can be isolated and described. The present study is not directly applicable to real engine installations but does, on the other hand, involve a wide range of fundamental flow features. With knowledge of these heat transfer mechanisms in practical installations are better understood and can thus be more efficiently improved.

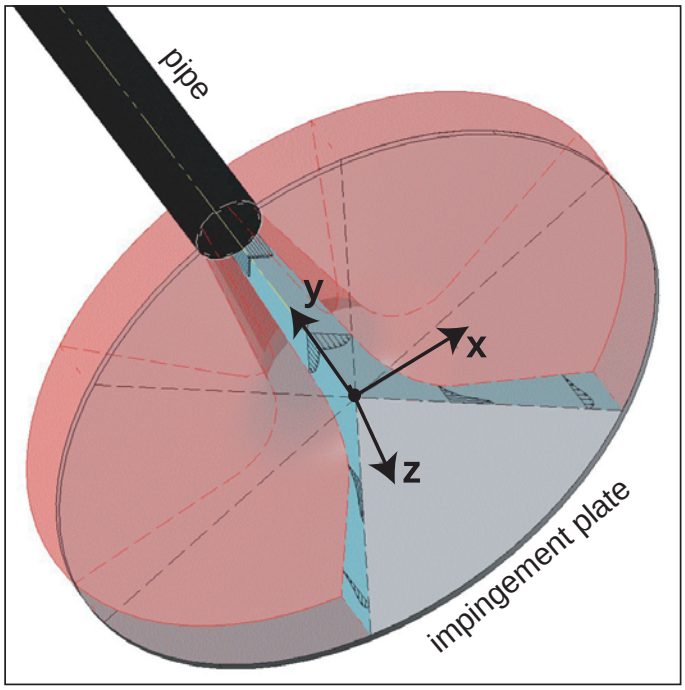

FIGURE 1.1. Illustration of a circular impinging jet. The flow emanates from a circular pipe and impinges onto a circular plate.

The impinging jet is an efficient tool in enhancing wall heat transfer (also mass transfer) and is therefore widely used in engineering applications. A typical impinging jet configuration is depicted in figure 1.1. The figure shows fluid flow that emanates from the nozzle of a pipe and impinges onto a circular flat plate. The flow at the nozzle outlet represents the inflow to the computation. The transparent surface represents an isosurface of the absolute velocity at low magnitude and the vectors in the cross sections depict a typical mean velocity field. The origin of the Cartesian coordinate system is located at the stagnation point. Common application areas of impinging jets are cooling of electrical components and gas turbine components, such as the combustion chamber and the turbine blades. It is also used in processing of metal and glass. In order to improve the process under consideration it is important to be familiar with its basic features. The heat transfer between the impingement wall and the ambient fluid depends on a large number of parameters. For instance, the ratio between the characteristic height and diameter of the jet is crucial for the development of the flow and has strong influence on the wall heat transfer. The

character of the incoming jet flow is also of great importance. Thus, the mean velocity profile, the fluctuating velocity field and the distribution of heat at the nozzle outlet (equivalently velocity inlet) are all essential for the behavior of the impinging jet. This is particularly so for cases where the nozzle is close to the target plate (less than $2-3$ diameters).

The main goal of this work has been to study and grasp the controlling factors and mechanisms related to the flow and heat transfer characteristics of impinging jets. Different geometries and flow configurations have been considered. For this Large Eddy Simulation (LES) featuring implicit filtering and implicit modeling has been used. The Sub-Grid-Scale effects are handled by an upwind-biased numerical scheme. The nozzle outlet has been supplied with different variants of inflow velocity profiles, ranging from top-hat profiles with superimposed random perturbations to fully developed pipe flow. The impingement surface is flat and orthogonal to the jet axis. As low temperature variations are considered the transport equation for a passive scalar has been used, neglecting effects of density variations.

The principal contributions of the present work are fourfold. Firstly, the dynamics of non-swirling and swirling impinging jets have been studied in some detail. These studies enhance the understanding of the coherent structures in the jet. These structures are important for entrainment and large-scale mixing. Secondly, the significance of inflow boundary conditions for the development of the flow and scalar fields has been elucidated for both free and confined jets. These studies have been performed for different inlet velocity profiles, superimposed with either random or periodic excitations, and for turbulent inflow conditions. Thirdly, the underlying mechanisms of impinging jet heat transfer have been identified, discussed and visualized. Fourthly, the implicit LES approach has proven to provide accurate results in an efficient manner. The simulation method is not problem dependent and is an alternative to conventional LES.

CHAPTER 2

Impinging jets

Even though the impinging jet constitutes a simple geometry it features extremely complex flow physics. This is partly so since the impinging jet involves three different flow regions: (a) free jet flow, (b) stagnation flow and (c) wall jet flow. These three flow regions are visualized in figure 2.1. The figure also depicts the normalized geometrical parameters D, H and W. Note that in the xy-plane at $z = 0$ (evaluation plane), x represents the radial direction, r, and z the azimuthal direction (cf. the orientation of the Cartesian coordinate system). The instantaneous velocity field in $\mathbf{x} = (x, y, z)$ is denoted by $\mathbf{u} = (u, v, w)$ and the mean velocity field is denoted by $\mathbf{U} = (U, V, W)$. The fluctuating velocity field is given by $\mathbf{u}' = \mathbf{u} - \mathbf{U}$. The flow and scalar fields at the inlet are defined by the normalized velocity V_{in}, the energy of the fluctuations k_{in} and the normalized concentration of temperature C_{in}. The concentration can, similar to the velocity, be decomposed as $c' = c - C$. For the normalization of the above parameters and of the computational results, appropriate combinations of the velocity-scale V_0 (mean inlet velocity), the length-scale D_0 (nozzle diameter) and concentration C_0 (mean inlet concentration) have been used. The Reynolds number (Re) is defined from the characteristic velocity- and length-scales. The vectors in the figure show a hypothetical velocity field. A true instantaneous velocity field of an impinging jet is not this structured but highly unsteady and features several demanding flow phenomena, such as e.g. instability, nonlinear vortex interactions, transition, vortex breakdown and separation. The computational process for an impinging jet is complex since the numerical code can, due to the multiple flow directions, not be optimized as efficiently as in case of free jets (see e.g. Danaila & Boersma 2000) and boundary layers.

Flow characteristics and wall heat transfer of conventional impinging jets depend strongly on a number of aspects, such as confinement, nozzle-to-plate spacing (H/D), nozzle geometry and flow conditions at the nozzle outlet (inflow conditions). This explains the significant amount of work devoted worldwide to this area of research. The fundamental aspect is the geometry of the problem, primarily with respect to the confinement plate. For a confined impinging jet the flow character and particularly the wall heat transfer change noticeably if H/D is smaller than, approximately, 0.5 (see e.g. Behnia *et al.* 1999). Also,

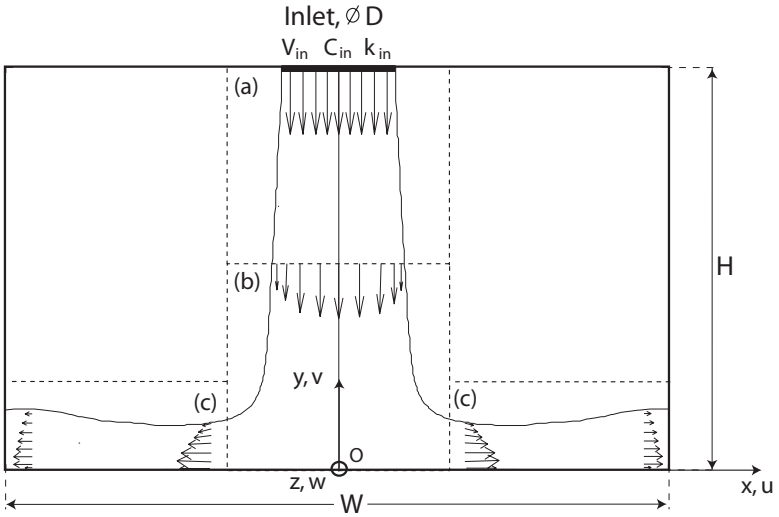

FIGURE 2.1. Geometry of the impinging jet, represented by the complete xy-plane at $z = 0$.

as shown in the work by Ashforth-Frost *et al.* (1997), confinement results in lower turbulence level within the axial jet and the potential core becomes, due to less entrainment and spreading of the jet, longer.

The most significant geometrical parameter is H/D since it is crucial for the flow character within, both, the axial jet and the wall jet. H/D is often put in relation to the length of the potential core as, for instance, the wall heat transfer, i.e. Nu, experiences (on average) two maximums if the impingement wall is located within the potential core. (This is however not always the case since the inflow conditions do also affect the character of the wall heat transfer.) Furthermore, as shown by Cornaro *et al.* (1999), for H/D less than two no discrete vortical structures are formed within the jet shear-layer. Instead the shedding of vortices occurs within the wall jet. For $H/D = 3$ large scale vortices, shed within the axial jet, are convected downstream. For $H/D = 4$, i.e. close to the length of the potential core, the shed vortices are, owing to breakdown and transition to turbulence, not as distinct within the wall jet as for $H/D = 3$. Of course, as stated above, this specific behavior is coupled to the considered initial conditions. For this particular case the inflow was created by a $10D$ long pipe at $Re = 6000$.

Except from wall heat transfer a change in flow characteristic, due to H/D, directly influences the wall shear stress (C_f). As shown by Yapici *et al.* (1999) both the magnitude of C_f and the radial location of the peak value changed

considerably with H/D. Maximum dimensionless friction was obtained for $H/D = 4$ at $r/D \approx 1$ ($Re = 9200$). As the distance increased beyond $H/D = 6$ (length of the potential core) the peak became wider and also displaced downstream. Naturally, also the wall pressure is influenced as H/D changes. As shown by Tu & Wood (1996) the wall pressure distribution was close to Gaussian and remained of similar shape as H/D was increased from 1 to 12 ($Re = 11000$). The dimensionless stagnation pressure ($C_{p_{stag}}$) remained on a constant level for H/D approximately less than 6. For larger H/D $C_{p_{stag}}$ decreased proportional to $(H/D)^{-1}$.

In order to construct empirical laws describing the average wall friction, wall pressure and wall heat transfer comprehensive parametrical studies have been performed throughout the years. The theoretical expressions based on Hiemenz flow solution or the division into separate regions, where approximations of the Navier-Stokes equations are valid, provide an estimate and are not generally applicable for practical applications. In the work by Tu & Wood (1996) the measured wall shear stress was compared to the Hiemenz solution (shear increases linearly with the distance from the stagnation point). The slope of C_f at the stagnation point was considerably steeper for the theoretical relation. In the work by Phares *et al.* (2000) the wall shear stress was derived analytically, for both fully developed slot and axisymmetric jets. By division of the flow field into four separate regions the magnitude and peak location of the shear stress was derived.

A great number of studies are aimed at determining the turbulent characteristics of the impinging jet. This is relevant not only with respect to the physical aspects but also with respect to assessment of turbulence models and numerical schemes. One of the more well known studies was performed by Cooper *et al.* (1993). They made hot-wire measurements of a fully developed circular impinging jet for nozzle-to-plate spacings within the range of $[2 \leq H/D \leq 10]$ and Reynolds numbers within the range of $[23000 \leq Re \leq 70000]$. Their results have been used for turbulence model assessment by, among others, Craft *et al.* (1993), Dianat *et al.* (1996), and Park & Sung (2001).

From a steady point of view (RANS approach) turbulent kinetic energy, k, is produced in the shear-layer of the axial jet, owing to the strong radial gradient of the axial velocity. The high level of k results in turbulent diffusion and thus increased jet spreading (e.g. mixing and entrainment). If H/D is large enough also the center region of the axial jet becomes turbulent. If not, the flow character within the stagnation region resembles that of the potential core. Near the stagnation point, production can in a two-dimensional perspective, by using continuity and ignoring shear stresses, be shown to be proportional to the difference between the two turbulent normal stresses. After deflection the flow develops into a wall jet involving one dominant mean flow gradient (wall-normal gradient of the radial velocity), that resumes the intense production of turbulence. Two wall parallel regions of production can be identified, one

in the outer and one in the inner part of the wall jet. Due to diffusion in the direction of the wall-normal gradient of k the two shear-layers merge and a turbulent wall jet forms. In the near-wall region production is mainly balanced by viscous dissipation. Even closer to the wall production goes, despite the strong mean flow gradient, towards zero. The origin to this is the negligible magnitude of k. The balance is here between terms proportional to the wall-normal gradient of k, i.e. viscous dissipation and viscous diffusion.

2.1. The free jet

The initial region of the impinging jet (region (a) in figure 2.1) is, for large enough nozzle-to-plate spacings, characterized by free jet behavior. A free jet can be defined as a jet entering a large container containing a quiescent fluid. Due to the radial spreading of the jet the axial velocity decreases continuously in the streamwise direction. The region of the jet in which the flow field is not affected by the growing annular shear-layer is called the potential core region. The flow in this region is essentially irrotational. The shear-layer grows in size in the downstream direction due to inherent shear-layer instability and vortex roll-up. Initially, if the disturbance level is very small, the shear-layer instability is similar to that described by Kelvin-Helmholtz linear stability theory.

The disturbances grow exponentially in the downstream direction why non-linear effects quickly become important and the linear approximation breaks down. As the disturbances grow large vortices start to roll up. These vortices (named vortices and not eddies due to their more coherent nature) grow in the downstream direction, increasing their length-scale. Simultaneously the range of scales increases through nonlinear interaction. A common process in the downstream direction is so-called vortex pairing, which strongly depends on the nature of the initial flow field (see e.g. Liu & Sullivan 1996; Hwang *et al.* 2001; Hwang & Cho 2003). Vortex pairing characterizes coalescence of two discrete vortices. The resulting larger vortex is referred to as the primary vortex (PV). Studies on the vortex pairing process in circular free jets have been conducted by, among others, Meyer *et al.* (1999).

At approximately four diameters downstream of the nozzle the free jet is fully developed and thereby the potential core is no longer present.[1] For an axisymmetric fully developed free jet the width of the mean axial velocity field, determined by the jet half-width[2], grows linearly as shown by e.g. Fondse *et al.* (1983), Cooper *et al.* (1993), and Hussein *et al.* (1994). Furthermore, the variation of the mean centerline velocity is independent of the Reynolds number and decreases proportional to x^{-1} for x/D larger than approximately

[1]The distance from the nozzle where a fully developed flow is reached differs from case to case due to the applied conditions at the nozzle outlet. Note that also the definition of fully developed turbulence differs from case to case.

[2]The jet half-width is the radial location at which the axial velocity is half of that at the centerline.

$4-6$ (see e.g. Crow & Champagne 1971; Hussein *et al.* 1994; Pope 2000), making the free jet develop in a self-similar manner. (Note that for the free jet the axial direction is represented by x, whereas for the impinging jet y represents the axial direction.) The radial velocity, which is much smaller than the axial, becomes self-similar in the far-field. Its magnitude can be directly maintained from the continuity equation. In the fully developed turbulent jet the Reynolds stresses also become self-similar (see Pope 2000). At the edge of the jet, the rms[3]-velocities are much larger than in the center-region. This is a consequence of the high levels of shear.

In the so-called self-preserving region of the jet the flow is not influenced by the nozzle exit conditions. At which distance from the nozzle the jet reaches this state is not clear as the results differ significantly within the literature. Some suggest the distance to be around $8D$ and some up to $70D$. In the work by Fondse *et al.* (1983) the influence from nozzle conditions on jet dynamics and jet self-preservation was studied. They concluded that if there exist an asymptotic jet state, independent of the nozzle conditions, it occurs at distances far larger than $20D$.

As the character of the annular shear-layer resembles that of boundary layers (main flow in the axial direction with weak axial gradients, weak mean flow in the radial direction with strong radial gradients of the axial velocity and homogeneity in the azimuthal direction) the simplified boundary layer equations can be employed. It can be shown that for increasing x the momentum ($\propto U^2$) is conserved, the kinetic energy ($\propto U^3$) decreases and mass flow ($\propto U$) increases. The latter is due to entrainment of ambient fluid. The conservation of momentum follows from the governing equations (momentum is often used to quantify the strength of the jet). The energy decreases as a consequence of dissipation and redistribution of momentum.

2.1.1. *Stability and structures of the free jet*

Several characteristic flow structures can be identified in the free jet. These are formed within the annular shear-layer. If the emanating jet is laminar (the disturbance level is within the linear regime) these structures originate from the above mentioned Kelvin-Helmholtz theory. One of the pioneering works on structures in jets was conducted by Crow & Champagne (1971). They studied the behavior of axisymmetric jets subjected to periodic forcing. The fundamental mode of the unforced laminar jet (Poiseuille profile), at a Reynolds number of $\mathcal{O}(10^2)$, was found to be the sinuous, i.e. spiral or helical mode. As Re was increased to $\mathcal{O}(10^3)$ the varicose, i.e. axisymmetric, mode became dominant (ring vortex). The axisymmetric structures remained also as the pipe boundary layer was tripped turbulent. In the more recent work by Danaila *et al.* (1997) the switch from the helical to the axisymmetric mode occurred

[3]The rms (root-mean-square) value defines the standard deviation of the dependent variable.

within the same range of Reynolds numbers as for Crow & Champagne (1971). The Strouhal number (based on the nozzle diameter and the mean velocity at the nozzle) of the fundamental mode ("jet-column mode"), detected by Crow & Champagne (1971), was found to be approximately equal to $St_D = 0.3$ ($\lambda \approx 2.4D$), independent of the Reynolds number [$\mathcal{O}(10^4) < Re < \mathcal{O}(10^5)$] and exit shear-layer conditions. Note that this frequency may vary widely between different experiments (see e.g. Liu & Sullivan 1996).

Without forcing and regardless of Re the maximum of the centerline fluctuation (u/U_e) was, within the work by Crow & Champagne (1971), attained at approximately eight diameters ($x/D \approx 8$) downstream of the nozzle. Active forcing of the fundamental mode augmented the vortical structures only upstream of $x/D \approx 8$, causing formation of an additional local maximum of u/U_e at $x/D \approx 4$. This maximum was due to the dynamics of the fundamental ($u_{0.30}/U_e$) and the superharmonic ($u_{0.60}/U_e$) modes. An increase of the disturbance intensity yielded higher value of $u_{0.30}/U_e$ and further upstream attained maximums. However, the response of the flow reached an asymptotic behavior at approximately five percent disturbance intensity. Without forcing the fundamental mode reached noticeable energy level downstream of two jet diameters whereas, for the superharmonic mode, growth was induced further upstream. Forcing of the fundamental mode was also found to promote the superharmonic mode. As shown by Ginevsky *et al.* (2004) low frequency forcing ($St_D = 0.32$) yielded strong amplification of the axisymmetric mode ($m = 0$) and high azimuthal correlation at ($x/D = 3, r/D = 0.24$). High frequency forcing ($St_D = 3.7$) yielded amplification of a broader spectral band, particularly the $m = 0$ and $m = 1$ modes, and low azimuthal correlation.

As shown by Crow & Champagne (1971) and Ginevsky *et al.* (2004) the dynamical character of the flow field is strongly affected by the applied forcing. This attribute can be used to achieve a jet of desired character, as active forcing at certain discrete frequencies may either promote or suppress the formation of vortical structures and turbulence. Thus, the mixing characteristics and noise generation in free jets can be controlled. Furthermore, as will be discussed later, active forcing is an efficient tool in achieving high rates of wall heat transfer for impinging jets. As shown by Raman *et al.* (1989) the excitability of the jet depends, among other things, on the initial turbulence level of the jet. In their experimental work they showed that the flow field was influenced by a small single frequency disturbance for up to 5% initial turbulence level. For higher turbulence level the jet was less influenced by forcing. They also concluded that the natural jet development was relatively unaffected by the initial turbulence level (within the range of $[0.15\% - 5\%]$).

Studies on suppression of turbulence in plane and circular jet flows have been performed by, among others, Zaman & Hussain (1981). They showed that the most unstable mode, with respect to the growth rate, of the circular jet equals a Strouhal number (based on the momentum thickness θ) of

$St_\theta \approx 0.017$. However, this frequency is not the characteristic one for the initial roll-up of vortices in the natural jet. The frequency for the initial roll-up equals a Strouhal number of $St_\theta \approx 0.012$ and represents the natural frequency of the system ("shear-layer mode"). In case of forcing of the most unstable mode there is quick growth and roll-up which results in early breakdown of the shear-layer why the formation of energetic vortices becomes suppressed. With no forcing the initial roll-up is slower why the shear-layer does not feature quick breakdown. The shear-layer mode grows in size and undergoes successive pairing why large energetic structures survive far downstream (delayed transition). When the jet was forced at the most unstable frequency maximum suppression of turbulence was achieved. The corresponding diameter based Strouhal number for suppression was in Zaman & Hussain (1981) concluded to be $St_D = 2.15$, which differs from values found in related work. They concluded that St_D was not a relevant parameter regarding shear-layer stability, instead St_θ must be considered. As stated by Hussain (1983) the axisymmetric mixing layer is characterized by two length-scales, i.e. the shear-layer thickness (θ) and the radius of curvature ($R = D/2$). The former scale is the relevant one if the diameter is significantly larger than the shear-layer thickness, i.e. in the initial stage of the jet ($x/D < 1$), and is the proper scaling for the shear-layer mode. Further downstream where the shear-layer becomes of same size as the jet diameter the latter scale is the relevant one and is the proper scaling for the jet-column mode.

The aforementioned suppression of discrete structures is a consequence of promoted shear-layer transition which obstructs the growth and successive pairing of discrete large scale vortices. The velocity fluctuations in the jet become dampened within an axial interval of approximately $[0.75 < x/D < 9]$ and the length of the potential core increases as a consequence of weaker entrainment. The entrainment of ambient fluid into the free jet is, as shown by Fondse *et al.* (1983) and Popiel & Trass (1991), primarily due to the development of large scale coherent structures (azimuthal vorticity). This suggests that laminar inlet conditions produce larger rate of entrainment than turbulent inlet conditions. With a turbulent boundary layer at the nozzle or if the flow is disturbed (e.g. mesh screen at the exit) coalescence of coherent structures is obstructed and, hence, the rate of entrainment decreases. For turbulent jets the entrainment is, as stated by Tritton (1988), a viscous process and thus determined by the small scales (for irrotational fluid to become rotational viscosity is needed). However, the large scales define the shape of the jet and consequently the interfacial area on which small turbulent scales act. The energy of the small scales is associated to the energy of the large scales why the entrainment process is indirectly determined by the large inviscid scales. As shown by Liepmann & Gharib (1992) entrainment is also greatly influenced by streamwise oriented structures. Downstream of the potential core, in the

turbulent regime, streamwise vorticity was found to be the main mechanism behind fluid entrainment.

A laminar unforced shear-layer exhibits an initial roll-up at the shear-layer mode (high frequency) whereas the jet-column mode (low frequency) is obtained further downstream, at the end of the potential core, as a result of successive pairing. The jet-column mode may also develop independently from the shear-layer mode. If the emanating jet is turbulent (practical jet) they typically roll-up at the jet-column mode and does not involve pairing (see Hussain 1983). As shown by Mi *et al.* (2001), fully developed flow at the nozzle outlet (achieved by a $72D$ pipe at $Re = 16000$) yielded no detectable formation of coherent structures within the jet shear-layer (at least for $x/D < 5$) whereas the laminar flow (achieved by smooth contraction) featured quick roll-up of axisymmetric structures ($St_D = 0.4$ at $x/D = 3$). The growth of the shear-layer was stronger in the laminar case.

In addition to the axisymmetric $m = 0$ mode there are different types of spiral or helical modes, i.e. the single helical modes ($m = \pm 1$) and the double helical modes ($m = \pm 2$). Hussain (1983) concluded that the initial disturbance found in their experiments was always of an axisymmetric character (downstream to $x/D \approx 3$). Furthermore, these axisymmetric structures could occasionally be tilted and therefore be interpreted as being helical. Petersen (1978) explained that the axisymmetric mode, for 2 to 6 diameters downstream of the nozzle, could appear, both visually and statistically, as helical due to obstruction of the azimuthal coherence by random straining ($Re_D = 5000 - 50000$). In more recent work it has been shown that in the fully developed region (jet far-field) of the natural circular jet the helical structures are the dominant ones. This was experimentally shown by, among others, Tso & Hussain (1989) ($Re_D = 69000$). However, as shown by Yoda *et al.* (1992) ($Re_D = 5000$) a few years later both modes are equally represented in the far-field of the natural jet. This conflict suggests that the development of the jet depends strongly on the nozzle outlet conditions and also on the choice of measurement technique. Yoda *et al.* (1992) also showed that any type of forcing, within a wide range of Strouhal numbers, favored the helical mode in the far-field of the jet. It has been found that also the initial region of the circular jet is equally sensitive to both axisymmetric and helical disturbances. Drubka *et al.* (1989) concluded that in the initial region of the laminar jet (laminar exit boundary layer) the two fundamental modes are approximately equally amplified. At $x/D = 0.5$ the energy level of these two modes were similar but with approximately 20% higher frequency for the $m = 1$ mode ($Re_D = 50000$). They concluded that there is temporal switching between the axisymmetric and the helical modes. At some instant of time the $m = 0$ mode could clearly be seen and at a later instant instead the helical mode was observed.

Linear stability analysis of circular jets have been conducted by e.g. Batchelor & Gill (1962), Morris (1976), Michalke & Hermann (1982), and Cohen &

Wygnanski (1987). Batchelor & Gill (1962) showed, among other things, that the fully developed jet (beyond the potential core) is unstable only to the helical mode (inviscid analysis). Michalke & Hermann (1982) showed in their inviscid analysis that the ratio between the radius of the jet and the momentum thickness was the relevant parameter (studied different *tanh* profiles). As this parameter decreases downstream, due to the diverging mean flow, the most unstable mode changes accordingly. For x/D less than approximately 2 the $m = 0$ mode exhibits maximum amplification and further downstream the $m = 1$ mode is the most unstable one. Morris (1976) stated that one should use realistic mean velocity profiles, i.e. not top-hat, for stability calculations. The disadvantage with realistic profiles is that, in most cases, no simple analytical solution exist. Also brought forward in his work was that for the hyperbolic-tangent profile the axisymmetric and helical modes are equally amplified. However, a small change in profile may make either of the modes dominant. Which mode that becomes dominant is also influenced by the initial perturbations. If the applied excitation is symmetric the axisymmetric mode will dominate a few diameters downstream.

In the work by Cohen & Wygnanski (1987) linear stability analysis was compared to experimental data. They found high correlation between the linear theory and the experimental results. Hence, their results confirm that viscous effects are not very important for the evolution of the jet. Furthermore, their results also showed that the divergence of the jet is of great importance for the development of the flow. Close to the nozzle, at $x/D = 0.5$, the ratio between the radius R and the momentum thickness θ is large. At this location the $m = 0$ mode and the first four helical modes exhibited similar growth rates. Further downstream the higher helical modes diminished, whereas the growth rates for the $m = 0$ and the $m = 1$ modes remained high and of similar level. At $x/D = 1$ the axisymmetric mode featured the strongest amplification. However, downstream from this location the $m = 1$ mode became more and more dominant. Also at high Reynolds number, i.e. fully developed turbulent flow, coherent structures seem to evolve in similar fashion as recently described. However, due to the fluctuations associated to the turbulent flow these structures are not as easy to detect.

The successive change of the dominant frequency in the jet is by some referred to as a continuous process and by some to as a step-like process (coalescence of vortices). Among others, Petersen (1978) and Popiel & Trass (1991) showed that the spacing, λ, between successive ring vortices grew linearly with the axial distance as $\lambda/D = 0.55x/D$. This can also be expressed as $\lambda/D = (U_c/U_0)St_D$, where U_c is the convection velocity, U_0 the exit velocity and St_D the diameter based Strouhal number. Thus, the vortex passing frequency changes proportional to $(x/D)^{-1}$. With $U_c/U_0 = 0.65$ the jet-column mode found by Crow & Champagne (1971) is attained at $x/D = 4$. As also

stated by Landa & McClintock (2004) the dominant frequency is, as a consequence of the divergence of the jet, monotonically decreasing with the distance from the nozzle outlet and does not behave as a step function. They explained that vortex pairing was not the cause of the decreasing frequency but rather a consequence. This was also concluded by Ho & Huang (1982).

In this work distinct vortex pairing is attained within the shear-layer of the axial jet for the top-hat profile and for the turbulent inflow conditions. At the location for pairing the dominant frequency halves and the wavelength doubles. But as can be seen from Hällqvist & Fuchs (2005*a*, 2006*a*) the subharmonic ($St_{n/2}$) is not a consequence of pairing as it contains energy also upstream of pairing, however with lower energy content than for the natural mode (St_n). Pairing is obtained at the spatial point where the subharmonic mode obtains similar energy level as the natural mode. The finding that paring is a consequence and not a cause agrees with the conclusions made by Landa & McClintock (2004). The discrepancy lies in the conclusion how the dominant frequency decreases (see Petersen 1978). However, a step-like behavior of the dominant frequency seems to be the most common description (see e.g. Zaman & Hussain 1981; Hussain 1983; Mankbadi 1985; Hwang *et al.* 2001; Ginevsky *et al.* 2004; Hsiao *et al.* 2004).

In the region between the successive ring vortices, called the braid region, secondary azimuthal instabilities grow which result in formation of counter-rotating streamwise oriented vortex pairs. The mechanism behind this is the stretching induced by the co-rotating ring vortices. These structures have been studied, by among others, Liepmann & Gharib (1992) and Brancher *et al.* (1994). There are also other types of instabilities present in free jets, such as side jets (see e.g. Brancher *et al.* 1994; Monkewitz & Pfizenmaier 1991). However, these kind of instabilities and structures are not the purpose of this thesis why they are not further discussed.

2.2. The wall jet

As for boundary layers the wall jet (see region (c) in figure 2.1) features a strong near-wall shear-layer in which the log-law applies, if the flow is fully developed. However, contrary to boundary layers the ambient velocity is not constant for large wall-normal distances. Instead there is a maximum in velocity at some distance from the wall, above which the velocity goes towards zero. Thus, wall jets feature, on average, two parallel shear-layers, among which the outer resembles of a free shear-layer. The outer shear-layer is inviscidly unstable as it features a point of inflection. If the boundary layer thickness is small relative to the azimuthal scale the wall jet takes on a two-dimensional character.

As shown by Chun & Schwarz (1967) and later by Cohen *et al.* (1992) the incompressible laminar two-dimensional wall jet features two coexisting unstable modes. The inviscid mode which governs large scale disturbances and the viscous mode which governs small scale disturbances. The viscous mode is

dominant in the near-wall region whereas the inviscid mode is dominant in the outer wall jet region. The latter is the more unstable one. The developing stage of the wall jet is strongly influenced by the initial conditions. In the work by Knowles & Myszko (1998) the wall jet was produced by an impinging jet and thus the initial conditions could be modified by changing the nozzle-to-plate spacing. By doing this the initial thickness and turbulence level of the wall jet can be controlled. Regardless of initial conditions the mean velocity of the wall jet reached self-similarity at $r/D = 2.5$, whereas the turbulent statistics became self-similar further downstream at $r/D = 4.5$. The outer shear-layer was shown to grow linearly as it evolved downstream.

In the work by Dejoan & Leschziner (2005) the evolution of a randomly perturbed laminar wall jet at $Re_b = 9600$ was treated by highly resolved LES. The wall jet showed a self-similar behavior at 20 discharge-nozzle heights (b). As the inner and outer shear-layers interact no evident distinction can be made regarding scaling. However, in the self-similar regime, the appropriate scaling in the inner layer is the friction velocity u_τ and ν/u_τ. In the outer the appropriate scaling is the maximum velocity and $y_{1/2}$, i.e the wall-normal distance at which the mean velocity (in the outer shear-layer) is half of the maximum.

2.3. Dynamical features of the impinging jet

Depending on the nozzle-to-plate spacing the dynamics in the proximal part of the impinging jet are as described in section 2.1. It should however be noted that it has been shown, by some authors, that as a target plate is introduced into the flow the large coherent vortices that impinge onto the plate may induce a feedback mechanism that triggers the flow at the nozzle outlet (self-sustained oscillations). This phenomenon may result in a change of the dynamical behavior. Note that it is plausible that the feedback mechanism is also relevant for free jets (see e.g. Rockwell & Naudascher 1979; Thomas & Goldschmidt 1985). The dynamics within the wall jet may deviate from that described in section 2.2 since the inlet conditions for the wall jet in the impinging jet configuration are determined by the upstream flow conditions. For pure wall jet studies the inlet conditions are often well defined and rarely of a quasi-turbulent nature.

The feedback mechanism (the origin to the resonance phenomenon) is of great importance for the dynamics of the jet if the induced pressure waves are of sufficient strength, i.e. of similar order as the inherent hydrodynamic instabilities. Acoustic resonance or feedback occurs for high speed impinging jets. As shown by Ho & Nossier (1981) resonance is obtained at mach number $M = 0.9$ but not at $M = 0.5$ (see also Umeda *et al.* 1987; Hourigan *et al.* 1996; Ginevsky *et al.* 2004). In the present study the velocity is considered to be low (a few meters per second, $M = \mathcal{O}(0.01)$) and therefore the flow is treated as incompressible. As pressure waves (acoustics) can not be captured by the incompressible approach the influence from this mechanism is omitted and has no influence on the results presented herein. This is justified by the low flow

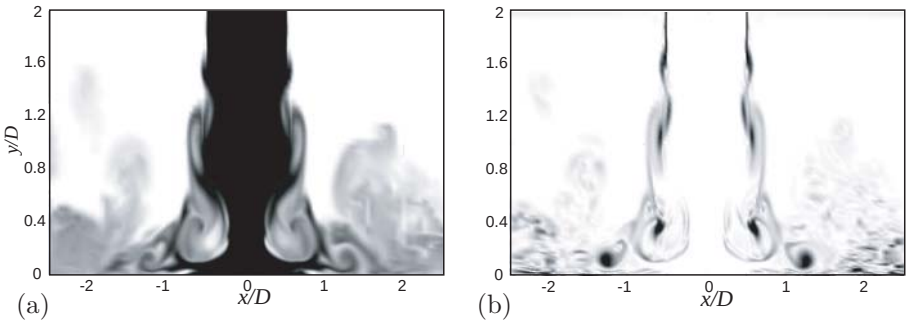

FIGURE 2.2. Instantaneous velocity field represented by scalar concentration in (a) and absolute vorticity in (b).

speed since this mechanism is only significant for high speed flows in which the acoustic wavelength is of the same order as H/D (see Rockwell & Naudascher 1979). In addition to the acoustic feedback there may be hydrodynamic feedback through the backflow (see e.g. Rockwell & Naudascher 1979; Thomas & Chu 1989; Maurel *et al.* 1996; Hsiao *et al.* 1999, 2004). Hence for impinging jets, the formation of coherent structures (in the shear-layer of the "free jet") may be influenced by the nozzle-to-plate spacing. However, from the experimental work by Popiel & Trass (1991) it can be concluded that the initial formation of vortices is not influenced by the presence of the impingement plate. As shown in the experimental work by Anderson & Longmire (1995) the vortex passing frequency, measured in the vicinity of the impingement wall ($0.02D$ above the wall), is slightly higher for the impinging jet than for the corresponding free jet. However, in the "free jet" region, above $1D$ from the wall, no effects from impingement was observed. This suggests that the feedback phenomenon is not relevant for the development of the flow in the initial region of the axial jet if H/D is larger than approximately one. The possible influences from this mechanism have not been considered within this work as the main focus is not on describing the sources of vortex formation, rather the consequences of vortex dynamics on wall heat transfer.

To get an understanding of the complex dynamics characteristic for impinging jets qualitative visualizations are depicted in figure 2.2. This figure depicts the instantaneous velocity field of an impinging jet featuring a top-hat profile subjected to periodic excitation. This specific case is chosen as it clearly illustrates the basic dynamical features of the flow. The instantaneous scalar concentration is shown in figure 2.2(a) and the instantaneous vorticity in figure 2.2(b). This specific case characterizes axisymmetric formation of vortices. Note that a symmetric vortex pair within the 2-D plane (symmetric around

$x = 0$) represents one axisymmetric ring vortex (toroid) in 3-D. At approximately $y/D = 1.2$ two individual ring vortices are closely located. As time progresses the vortices will coalesce and form one larger discrete ring vortex, a so-called primary vortex. Primary vortices, formed from pairing, can be seen further downstream in the flow. The significant local thinning of the axial jet core just upstream of impingement in figure 2.2(a) is associated to the large scale ring vortex seen in figure 2.2(b). If the nozzle-to-plate spacing would have been larger this vortex would, at a location further downstream, completely absorb the potential core. Within the wall jet, downstream of $|x/D = 1|$, a sharp symmetrical ring vortex is located. This vortex has initiated formation of a counter rotating secondary vortex (SV), which in turn, at a later instant of time, may cause local flow separation (see Hällqvist & Fuchs 2005*b*). Further downstream the energy of the discrete vortices decreases and finally, as they break down, they are completely absorbed by the surrounding flow. At this stage there are no evident discrete modes present and the flow is hence considered to be fully turbulent.

Illustrative pictures of the impinging jet flow field can also be found in the experimental studies by, among others, Popiel & Trass (1991), Anderson & Longmire (1995), Cornaro *et al.* (1999), and Angioletti *et al.* (2003) and in the numerical study by e.g. Tsubokura *et al.* (2003).

Analysis and control of the vortical structures formed within circular impinging jets were performed by Liu & Sullivan (1996). In their experiment the natural frequency was, at a Reynolds number of 12300, measured to be $St_\theta = 0.016$. This corresponded to a diameter based Strouhal number of $St_D = 1.23$. Further downstream the vortex passage frequency changed in a stepwise manner to $St_D = 0.61$. They concluded that the natural frequency of the impinging jet was the same as for the free jet if $H/D > 1.1$. For smaller H/D the presence of the wall resulted in an increase of the frequency. Hence, one can conclude, also from this work, that impingement has no influence on the formation of vortices. Implying that there is no influence from feedback mechanisms on the initial flow field, when H/D is larger than approximately one jet diameter. Both Liu & Sullivan (1996) and Cornaro *et al.* (1999) showed that for small spacing, $H/D = 1.125$, no large scale vortices were formed within the annular shear-layer. Instead, vortices were shed as the flow was deflected by the wall. Downstream within the wall jet pair of vortices merged. Depending on the forcing frequency the character of vortex pairing changed (see Liu & Sullivan 1996). When forced close to the subharmonic of the natural frequency ($St_e \approx 0.83$) stable pairing was obtained (St_e is the diameter based forcing or excitation frequency). When forced at a higher frequency ($St_e \approx 1.53$) intermittent vortex pairing was obtained. In the former strong counter rotating secondary vortices were formed (in turn inducing unsteady separation) whereas in the latter less organized eddy-like structures were formed.

The formation of counter rotating secondary vortices and wall separation was observed for more than three decades ago by Harvey & Perry (1971). Later Didden & Ho (1985) made detailed studies on unsteady separation produced by an impinging jet. They showed that the boundary layer separated periodically as a consequence of the, by the primary vortices, induced unsteady adverse pressure gradient. They found that the convection speed of the primary vortices was the same in the wall jet and in the annular shear-layer of the axial jet ($U_c = 0.61U_0$). However, the induced secondary vortices were convected at 20% higher speed. By means of PIV Landreth & Adrian (1990) studied the instantaneous flow field of a circular impinging jet at $Re = 6564$ and $H/D = 4$. They observed an abrupt increase of the wall boundary layer thickness at approximately two diameters downstream of the stagnation point. From these results they concluded that secondary vortices consistently break away from the wall jet. The secondary vortices were formed close to $r/D = 1.8$.

Recently Hall & Ewing (2005) studied the influence from Reynolds number ($Re = 23300$ and $Re = 50000$) on the formation and three-dimensionality of vortical structures present in a fully developed circular impinging jet with a nozzle-to-plate spacing of two. They showed that the normalized contribution from azimuthal modes were approximately equal for the two considered Reynolds numbers. However, from frequency spectrums it was observed that large-scale structures were more prominent and of a more periodic character for the high-Re case. The convection velocity for the large scale structures was similar in both cases. The breakdown of structures in the radial direction was, judging from the integral length-scale in the azimuthal direction, slightly more pronounced in the high-Re case.

2.4. Heat and mass transfer of the impinging jet

The impinging jet is probably most acknowledged for its capability in achieving significant rates of wall heat transfer (or equivalently mass transfer). This is why impinging jets are widely used for cooling and heating in practical engineering applications. The heat transfer from or to the target plate (quantified by the Nusselt number, Nu) is, from an average perspective, influenced by three mechanisms. These are: convection by the mean flow, turbulent transport and molecular diffusion. Instantaneously there are only two mechanisms present, i.e. convection by the unsteady flow and molecular diffusion. As buoyancy effects are assumed to be negligible the transport of heat is directly determined from the known velocity field. If the flow is strongly convective (diffusion being negligible) heat behaves as a tracer. Under these circumstances smoke visualizations can be used to characterize the dynamics of the flow. If diffusive effects need to be accounted for, i.e. diffusive time-scale comparable to the convective, smoke visualizations do not provide the true picture of the flow. This is the case also in the wall region of convection dominated flows, where

diffusive effects are dominant. Some of the basic aspects of impinging jet heat transfer can be found in the work by Arganbright & Resch (1971).

As described before the geometrical parameter H/D is of great importance also for Nu. If the spacing is larger than the length of the potential core a fully developed jet will impinge onto the wall, i.e. turbulent jet impingement. Due to a high level of turbulent kinetic energy (k) within the center region of the axial jet maximum heat transfer is obtained at the stagnation point. From the stagnation point and downstream Nu decreases monotonically. If the potential core is longer than H/D the initial region of the wall jet becomes laminar-like, featuring low levels of k. Thus, the Nusselt number experiences a local minimum at the stagnation point (saddle shape). As the laminar-like wall jet accelerates wall shear increases, due to thinning of the velocity boundary layer, and a local maximum of C_f is obtained at approximately $r/D = 1/2$. As the flow is laminar the maximum in wall friction is accompanied by a maximum in wall heat transfer. From this maximum and somewhat downstream Nu decreases. Further downstream the range of scales has grown large and the wall jet becomes turbulent. This results in a second maximum of Nu. Note that the second maximum is also influenced by large organized structures. These coherent structures may also obstruct the formation of a second maximum (see e.g. Liu & Sullivan 1996). Maximum stagnation heat transfer is attained when the nozzle-to-plate spacing is about $6-8$ nozzle diameters long (see e.g. Baughn & Shimizu 1989). For smaller H/D the level of k is the limiting factor and for larger H/D the axial momentum is the limiting factor.

The wall heat transfer is strongly influenced by the dynamics of the unsteady velocity field. Generally lumps of chaotic eddies have a positive effect on wall heat transfer whereas large ordered structures may, depending on the sense of rotation, have a promotive or obstructive effect. To clarify this the transfer of heat to or from the wall may be divided into contributions from: (1) the mean flow, (2) coherent structures, (3) chaotic structures (turbulence) and (4) molecular diffusion. This division of sources was made by Liu & Sullivan (1996) in their study of excited circular impinging jets. They concluded that when intermittent vortex pairing was promoted the induced large amount of chaotic structures yielded a second maximum of the Nusselt number at $r/D = 1.5 - 1.8$. For stable vortex pairing the induced organized large scale structures had locally a negative effect on wall heat transfer, owing to unsteady separation and decreased mean shear (Reynolds analogy: $Nu \propto C_f$). Active control of wall heat transfer was also conducted by Hwang *et al.* (2001) and Hwang & Cho (2003). Contrary to Liu & Sullivan (1996) vortex pairing was obtained within the free jet shear-layer. Promotion of vortex pairing resulted in shorter potential core and thus higher Nu for small H/D and lower Nu for large H/D. Suppression of vortex pairing gave the opposite effect. Furthermore, the secondary maximum (for $H/D = 4$) moved downstream as vortex pairing was suppressed.

A change in Reynolds number has larger influence on wall heat transfer for small H/D than for large. As shown by Angioletti *et al.* (2003) stagnation point heat transfer increased by 15% when Re was changed from 1500 to 4000 for $H/D = 4.5$. The same change for $H/D = 2$ resulted in a 56% increase. For the smaller spacing there were also more pronounced changes in the relative distribution of Nu. A second peak of Nu was only obtained for the higher Re case. As shown by, among others, Tawfek (1996) and Chan *et al.* (2002) the normalized stagnation point heat transfer increases linearly with increasing Reynolds number for all considered values of H/D.

Based on laminar flow theory Shadlesky (1983) derived a relation for the stagnation point Nusselt number which is valid for axisymmetric jets: $Nu_0 = 0.585(Pr)^{0.4}(Re_D)^{1/2}$. This relation holds for small nozzle-to-plate spacings for which the stagnation flow is laminar. Chan *et al.* (2002) found that the Re-dependence on the stagnation Nusselt number increased as H/D became larger than the potential core ($Re^{0.54}$ instead of $Re^{1/2}$). The considered range of Reynolds numbers was $[5600 \leq Re \leq 13200]$. Due to the changing character of the wall jet Viskanta (1993) found that Nu was proportional to $(Re_D)^{1/2}$ downstream to $r/D = 2$ and to $(Re_D)^{0.7}$ for larger radii. A more complete relation was derived by Tawfek (1996), in which the average Nusselt number scales as: $Nu = 0.453(Pr)^{1/3}(Re_D)^{0.691}(H/D)^{-0.22}(r/D)^{-0.38}$. This relation holds for $[2 \leq r/D \leq 30]$, $[6 \leq H/D \leq 58]$ and $[3400 \leq Re_D \leq 41000]$.

In order to assess high wall heat transfer it is, as discussed above, important to pay attention to the inflow conditions (mean profile and perturbations) and the nozzle-to-plate spacing of the impinging jet. Further improvements of the wall heat transfer can be achieved by modification of the surface conditions (see e.g. Baukal & Gebhart 1997; Beitelmal *et al.* 2000) or by installing perforated plates prior to impingement (see Lee *et al.* 2002*a*). The shape of the nozzle outlet has also large influence on the wall heat transfer, particularly for small H/D (see e.g. Colucci & Viskanta 1996; Garimella & Nenaydykh 1996; Brignoni & Garimella 2000; Lee & Lee 2000*a*,*b*).

2.5. Swirling impinging jets

A swirling free jet involves the same basic features as the non-swirling free jet, characterizing a fundamental Kelvin-Helmholtz instability. However, additional instabilities are introduced by the azimuthal velocity component. These instabilities may be due to centrifugal instability (see e.g. Billant *et al.* 1998). As shown by Panda & McLaughlin (1994) the overall growth of instability waves in swirling jets is, as a consequence of the quick growth of the momentum thickness, weaker why vortex pairing becomes suppressed (compare with the R/θ ratio for free jets above). This results in less distinct coherent structures and promotion of the transition to turbulence. For a swirling jet the spreading and entrainment rates are higher relative to a non-swirling jet. In the latter case

entrainment is associated to the large scale coherent structures. These however are not present in strongly swirling flows why an alternative explanation is needed. The high rate of entrainment may originate from the strong radial pressure gradient which is induced to balance the centrifugal force. It may also be influenced by centrifugal instabilities.

For a strongly swirling jet a recirculation bubble is formed that may cause reversed flow also at the nozzle exit (see Komori & Ueda 1985). This phenomenon (vortex breakdown or vortex bursting) is, as stated by Panda & McLaughlin (1994), the origin to the promoted transition. As the flow field, induced by the vortex breakdown, interacts with the annular shear-layer rapid transition to turbulence is obtained. Within two diameters downstream of the nozzle outlet the jet becomes fully turbulent. Vortex breakdown occurs at a specific critical swirl number and is defined as the formation of a central recirculation zone (backflow in the core region). It should be noted that in addition to the swirl number (which may be defined in different ways), also the radial distribution of the velocity profiles is important. Generally speaking, the swirl number, independently of its definition, is not adequate to characterize the swirling jet flow (see Hällqvist & Fuchs 2006*b*). As shown by Panda & McLaughlin (1994) the size, shape and location for breakdown change strongly with the Reynolds number. For sufficiently high *Re* breakdown occurred within the nozzle. For a free circular swirling jet there are several different modes or states of breakdown, i.e. pronounced structural change. As shown by Sarpkaya (1971) there are basically, depending on the Reynolds number and swirl number, three types of vortex breakdown. One of these is the axisymmetric breakdown, where an axisymmetric recirculation bubble is formed. The flow then becomes stabilized and then breaks down a second time forming a helical shape. Billant *et al.* (1998) studied the characteristics of various breakdown states. They identified four distinct forms of vortex breakdown. These include the, above mentioned, bubble and helical modes.

Lee *et al.* (2002*b*) performed experimental work on a swirling round impinging jet with heat transfer. They concluded that the effect of the swirling jet flow was mainly represented in the near stagnation region and that the averaged Nusselt number became lower for increasing swirl numbers. For larger radial distances ($r/D > 2$) the effect from swirl was negligible. Huang & El-Genk (1998) also made experimental studies on swirling impinging jets. They found, similar to Lee *et al.* (2002*b*), that the swirl velocity influenced the level of wall heat transfer and location of the second peak in Nusselt number. In both these works there is comparison with conventional non-swirling circular impinging jets. Comparison with conventional jets for small nozzle-to-plate spacing may be somewhat misleading as the commonly used swirl generators (see also Wen & Jang 2003) produce multiple jet impingement. Multiple jets feature, due to additional shear, higher level of turbulence. This contributes to an augmentation of the wall heat transfer. Contrary to the results for Lee

et al. (2002*b*), Wen & Jang (2003) concluded that the wall heat transfer was augmented with applied swirl. Maximum effect was found at high Reynolds number ($Re = 27000$) and small H/D.

Instead of using swirl generators it is possible to generate a swirling jet by using a long rotating pipe. However, this is a much more demanding experimental setup. This type of setup was used by Imao *et al.* (1996). They made experimental studies of turbulence characteristics in a rotating pipe using LDV. This setup has also been used by Facciolo (2003) to study the turbulent characteristics in the rotating pipe and in the turbulent swirling jet.

The studies of swirling impinging jets in this thesis are conducted for small nozzle-to-plate spacings and at a Reynolds number of 20000. Two different types of inflow conditions have been considered. The first one is a simple top-hat profile with superimposed solid body rotation. The second one originates from a precursor simulation of rotating turbulent pipe flow. The influence from three different swirl levels on the flow field and on the wall heat transfer has been studied in this thesis (see Hällqvist & Fuchs 2004, 2005*c*, 2006*b*).

CHAPTER 3

Theory and governing equations

3.1. Basic equations

The motion of incompressible fluids is fully described by four governing equations, i.e. the continuity equation and the momentum equations. The latter ones are commonly refereed to as the Navier-Stokes equations (NS). The continuity equation is derived from the physical principle of conservation of mass, stating that the time rate of change of the mass of a fluid element is zero. Using Cartesian tensor notation and Einstein's summation convention, the continuity equation can be written as

$$\frac{\partial u_i}{\partial x_i} = 0. \tag{3.1}$$

The momentum equations are based on Newton's second law which states that the time rate of change of momentum of a fluid element equals the sum of forces exerted on it. With the assumption of a Newtonian fluid, see equation (3.8), the momentum equations take the following form

$$\frac{\partial u_i}{\partial t} + \frac{\partial}{\partial x_j}(u_i u_j) = -\frac{1}{\rho}\frac{\partial p}{\partial x_i} + \nu \frac{\partial}{\partial x_j}\frac{\partial u_i}{\partial x_j}, \tag{3.2}$$

here expressed in conservative dimensional form. The subscripts i and j represent the components/directions in configuration space and can take values between one and three, i.e. $i, j = 1, 2, 3$. By setting $t = t^* D_0/V_0$, $u = u^* V_0$ and $x = x^* D_0$ the momentum equations can, after dropping the superscript $(^*)$, be written in dimensionless form as

$$\frac{\partial u_i}{\partial t} + \frac{\partial}{\partial x_j}(u_i u_j) = -\frac{\partial p}{\partial x_i} + \frac{1}{Re}\frac{\partial}{\partial x_j}\frac{\partial u_i}{\partial x_j}, \tag{3.3}$$

where V_0 is the characteristic velocity, D_0 the characteristic length-scale of the flow and Re is the Reynolds number. This is a dimensionless number defined as

$$Re = \frac{V_0 D_0}{\nu}, \tag{3.4}$$

where ν is the kinematic viscosity of the fluid. The Reynolds number defines the ratio between inertia forces and viscous forces.

Fluid motion can be decomposed into translation, rotation and deformation. The translation is given by the velocity itself. The two latter ones are defined by the symmetric and the antisymmetric part, respectively, of the velocity gradient tensor $u_{i,j}$ as

$$\frac{\partial u_i}{\partial x_j} = S_{ij} + \Omega_{ij}. \tag{3.5}$$

The symmetric part is the deviatoric strain rate tensor

$$S_{ij} = \frac{1}{2}\left(\frac{\partial u_i}{\partial x_j} + \frac{\partial u_j}{\partial x_i}\right), \tag{3.6}$$

and the antisymmetric part is the rate of rotation tensor

$$\Omega_{ij} = \frac{1}{2}\left(\frac{\partial u_i}{\partial x_j} - \frac{\partial u_j}{\partial x_i}\right). \tag{3.7}$$

The strain rate tensor S_{ij} can be further decomposed into one isotropic part and one traceless part. The former describes the rate of change of the volume of the fluid element and the latter describes pure deformation. In a Newtonian incompressible fluid the stress within the fluid is given by

$$T_{ij} = -p\,\delta_{ij} + \tau_{ij} = -p\,\delta_{ij} + \mu\left(\frac{\partial u_i}{\partial x_j} + \frac{\partial u_j}{\partial x_i}\right), \tag{3.8}$$

where T_{ij} is the total stress tensor and τ_{ij} the viscous stress tensor, which is linearly related to the strain rate tensor.

From the rate of rotation tensor the vorticity of a fluid element can be written as

$$\omega_i = \varepsilon_{ijk}\frac{\partial u_k}{\partial x_j}, \tag{3.9}$$

where the subscript $i = 1, 2, 3$ defines the coordinate direction. Vorticity can not be created in inviscid flows as shear forces are absent. In order for the

initial vorticity to arise viscous effects are mandatory. However, the rate of vorticity can change also in inviscid flows through vortex tilting and vortex stretching. These mechanisms are only present in three-dimensional flows. By tilting vorticity is transformed from one direction to another direction. By stretching the moment of inertia decreases and thus, due to conservation, the vorticity increases. Stretching can also be negative, i.e. the vorticity decreases whereas the moment of inertia increases.

An important parameter for practical applications is the force exerted by the flow on a solid wall. This force depends on the wall shear stress (τ_w)

$$\tau_w = \mu \left(\frac{\partial u}{\partial y} \right)_{y=0}, \tag{3.10}$$

where $\partial u/\partial y$ is the wall-normal derivative of the wall parallel flow velocity. From the wall shear stress it is possible to define the dimensionless skin friction coefficient as

$$C_f = \tau_w / \left(\frac{1}{2} \rho V_0^2 \right). \tag{3.11}$$

As this coefficient is based on the wall-normal derivative it is difficult to accurately asses, both experimentally and computationally.

3.2. Turbulence

The Reynolds number defined in the previous section can be used to classify the state of the flow. Low values of Re correspond to typically low speeds or small length-scales. In these cases the flow is structured and ordered, known as laminar flow. For Reynolds numbers larger than some certain critical value, Re_{crit}, that depends on the particular flow, the flow becomes irregular and ultimately, with increasing Re, turbulent. The stability of laminar flows are often analyzed by linear stability analysis. Linearization of the Navier-Stokes equations is done by introducing small perturbations and neglecting second order terms. This method has successfully been used to predict the critical Reynolds number for different (simple) flows. For boundary layer flows the critical Reynolds number is reached at some downstream location, x_{crit}. The region downstream of x_{crit} is called the transition region. As the Reynolds number increases even more, due to the increase of x, the flow develops into fully turbulent flow. The Reynolds number at which the flow changes character is called the transition Reynolds number, Re_{tr}. The turbulence becomes fully developed only at some higher Re. The nonlinearity of the Navier-Stokes equations make it impossible to analytically describe the transition process nor fully turbulent flow fields.

Turbulence is said to be one of the principal unresolved problems in physics today. Turbulence is characterized by the following features:

- *Irregular* - the fluid motion is chaotic, making statistical methods the only possible approach for description of the flow.
- *Dissipative* - viscous forces continuously transfer turbulent kinetic energy into heat, therefore turbulence needs a balancing supply of energy to persist.
- *Diffusive* - high rates of mixing, efficient in transporting momentum and heat.
- *Three-dimensional and time dependent* - turbulence is three-dimensional and features high levels of fluctuating vorticity. The vorticity fluctuations depend on a process called vortex stretching. This process is absent in two-dimensional flows. All turbulent flows are rotational.
- *Continuum* - even the smallest turbulent scales are much larger than the mean free path, i.e. mean molecular distance.
- *Property of the flow* - turbulence is a feature of the flow and not the fluid.

The velocity and size of the large rotational flow structures constitute the largest eddies of the turbulent flow. These eddies are characterized by a velocity of the same order of magnitude as the typical velocity-scale V_0 and by a typical length-scale D_0, which is of the order of the mean flow. The large scales of the eddies are frequently referred to as the integral velocity-scale u_0 and the integral length-scale ℓ_0, respectively. Thus, the energy of the large eddies is proportional to u_0^2. Kolmogorov's theory implies that the turbulent kinetic energy, extracted from the mean flow, is transferred through a cascade of smaller and smaller scales down to the smallest dissipative scales. Kolmogorov's theory is valid for very large Re. By considering dissipation effects one can show that even if the large-scale fluctuations are non-isotropic (since these depend on the particular problem and boundary conditions) the smaller scale statistics are isotropic in character. (Isotropic turbulence implies that statistical quantities are directionally independent.) The larger eddies behave very much as in an inviscid fluid, i.e. viscous dissipation is not relevant. On the other hand, the smallest scales of turbulence, the so-called Kolmogorov length-, velocity- and time-scales are determined by the viscosity ν and the viscous dissipation ε. The Kolmogorov scales can be determined by dimensional analysis and are

$$\eta = \left(\nu^3/\varepsilon\right)^{1/4}, \tag{3.12}$$

$$u_\eta = (\varepsilon\nu)^{1/4}, \tag{3.13}$$

$$\tau_\eta = (\nu/\varepsilon)^{1/2}. \tag{3.14}$$

The Reynolds number based on these scales equals unity

$$\frac{u_\eta \eta}{\nu} = 1. \tag{3.15}$$

The dissipation, ε, can be estimated as

$$\varepsilon = \nu(u_\eta/\eta)^2 = \nu/\tau_\eta^2. \tag{3.16}$$

For turbulence in equilibrium (dissipation equals production) one may estimate the dissipation of turbulent kinetic energy by the integral scales as

$$\varepsilon \sim u_0^3/\ell_0. \tag{3.17}$$

In terms of the integral scales and the turbulent Reynolds number ($Re = u_0\ell_0/\nu$) one may express the Kolmogorov scales as

$$\frac{\ell_0}{\eta} = \mathcal{O}(Re^{3/4}), \tag{3.18}$$

$$\frac{u_0}{u_\eta} = \mathcal{O}(Re^{1/4}), \tag{3.19}$$

$$\frac{t_0}{\tau_\eta} = \mathcal{O}(Re^{1/2}). \tag{3.20}$$

The wide range of length-scales ℓ can be divided into three regions in accordance to figure 3.1. The energetic region contains the largest eddies (larger than approximately $\ell = \ell_0/6$). The inertial subrange region contains scales from approximately $\ell = \ell_0/6$ down to scales of the order of $\ell = 60\eta$. According to Kolmogorov the spectrum in this range is determined by the wavenumber (eddy size) and the dissipation of turbulent kinetic energy . By dimensional arguments one finds that the spectrum of the turbulent kinetic energy is

$$E(\kappa) = C_k\, \varepsilon^{2/3}\kappa^{-5/3}, \tag{3.21}$$

where κ is the wavenumber, defined as $2\pi/\ell$, and C_k is the Kolmogorov constant. This relation applies only in the inertial subrange region for Reynolds numbers tending to infinity, i.e. the influence from energetic scales and mean strain can be ignored. The far range of the spectrum, which contains the smallest scales (smaller than about $\ell = 60\eta$) belong to the dissipative subrange. Kolmogorov's theory assumes universal spectral behavior (in the inertial and the dissipative ranges). It also assumes that turbulence is in equilibrium. The two

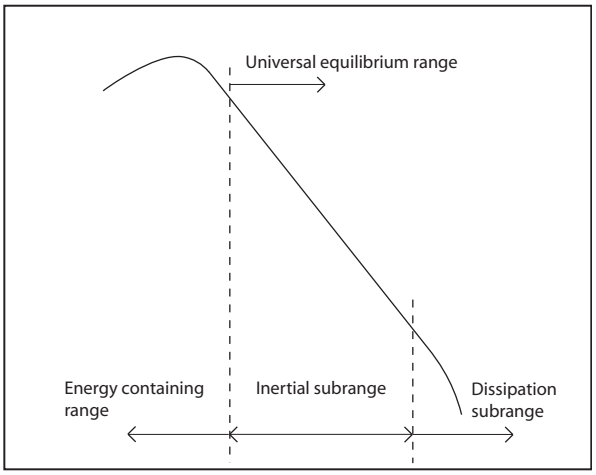

FIGURE 3.1. Energy spectrum for fully developed high-Re turbulence.

universal ranges of scales are by definition termed as the universal equilibrium range.

The time- and length-scales of turbulent flows can be determined by using data of statistical character. The correlation of a variable with itself, at any given point in space, is the so-called time autocorrelation function and is defined as

$$\rho(s) = \overline{u'(t)\, u'(t+s)} \;/\; \overline{u'(t)^2}, \tag{3.22}$$

where the *prime* indicates a fluctuating component and s is the lag time. This quantity can be used to calculate the integral time-scale of the flow as

$$t_0 = \int_0^\infty \rho(s)\; ds. \tag{3.23}$$

The integral time-scale is a measure of how long time the u' variable is highly correlated with itself, i.e. a measure of the memory of the flow. The corresponding correlation in space (for each time instant and in the direction of the velocity component) is termed as the longitudinal autocorrelation and is given by

$$f(\xi_1) = \overline{u_1'(x_1)\, u_1'(x_1+\xi_1)} \;/\; \overline{u_1'(x_1)^2}, \tag{3.24}$$

where ξ_1 is the separation in the x_1 direction. A corresponding expression can be defined for the transversal correlation (with the distance vector normal to the velocity direction). From the space autocorrelation one may define the integral longitudinal length-scale as the mean interaction distance according to

$$\ell_0 = \int_0^\infty f(\xi_1)\ d\xi_1. \tag{3.25}$$

If the local convection velocity U_c is more or less unaffected by the turbulent fluctuations one can relate time and space correlations by Taylor's hypothesis,

$$\frac{\partial}{\partial t} = U_c \frac{\partial}{\partial x}. \tag{3.26}$$

This relationship makes it possible to evaluate more relevant two point space correlations from the easier measured one point time correlations.

Viscous dissipation transforms turbulent kinetic energy of the flow into internal energy, i.e. heat. This is due to the fluctuating velocity gradients $\partial u_i'/\partial x_j$, working against the deviatoric stresses $2\nu s_{ij}'$, where s_{ij}' is the fluctuating strain rate. The complete dissipation of turbulent kinetic energy is defined as

$$\varepsilon = 2\nu\overline{s_{ij}' s_{ij}'}, \tag{3.27}$$

and is by definition always positive. The dissipation is often approximated as

$$\varepsilon = \nu\overline{u_{i,j}' u_{i,j}'}. \tag{3.28}$$

Turbulent flow fields are often analyzed in terms of the Reynolds stress equation. This equation describes the time rate of change of the Reynolds stresses, R_{ij} (also $\overline{u_i' u_j'}$). The Reynolds stress equation can be written as

$$\frac{\partial R_{ij}}{\partial t} + U_k \frac{\partial R_{ij}}{\partial x_k} = \mathcal{P}_{ij} - \varepsilon_{ij} + \Pi_{ij} - \frac{\partial}{\partial x_m}\left(J_{ijm} - \nu\frac{\partial R_{ij}}{\partial x_m}\right), \tag{3.29}$$

where $\mathcal{P}_{ij}$ is the production tensor

$$\mathcal{P}_{ij} = -\overline{u_i' u_k'}\frac{\partial U_j}{\partial x_k} - \overline{u_j' u_k'}\frac{\partial U_i}{\partial x_k}, \tag{3.30}$$

and ε_{ij} is the dissipation tensor

$$\varepsilon_{ij} = 2\nu \overline{\frac{\partial u_i'}{\partial x_k} \frac{\partial u_j'}{\partial x_k}}. \tag{3.31}$$

The third term on the right hand side of equation 3.29 is referred to as the pressure-rate-of-strain tensor and represents redistribution of energy among the components. This tensor has zero trace and has thus no influence on the equation for the turbulent kinetic energy. The first term inside the parenthesis represents transport due to the fluctuating pressure (pressure transport) and the fluctuating velocity (turbulent convection). The second term inside the parenthesis represents viscous diffusion. By taking half the trace of the Reynolds stress equation the transport equation for the turbulent kinetic energy is obtained. This equation is often used in (RANS) turbulence modeling context (one- and two-equation models).

3.3. Basics of heat and mass transfer

If the flow field can be assumed to be unaffected by variations in temperature or variations in concentration the transport equation for a passive scalar can be used to represent heat or mass transfer. The instantaneous scalar concentration is denoted by c. The scalar is assumed to be advected by the fluid in addition to molecular diffusion (that obeys Fourier's- or Fick's-law). Thus, the transport equation for c can be expressed as

$$\frac{\partial c}{\partial t} + u_j \frac{\partial c}{\partial x_j} = \Gamma \frac{\partial^2 c}{\partial {x_j}^2}. \tag{3.32}$$

In this equation Γ represents the diffusivity and defines the significance of molecular effects, i.e. same interpretation as viscosity in equation (3.2). If c represents temperature Γ represents the thermal diffusivity α. If the kinematic viscosity is put in relation to the thermal diffusivity one obtains the Prandtl number as $Pr = \nu/\alpha$. The Prandtl number is a dimensionless number representing the ratio of diffusion of momentum to diffusion of heat. For boundary layer flows of fluids with Pr close to unity the thermal boundary layer is of the same size as the velocity boundary layer. In air at room temperature the Prandtl number is equal to 0.72, meaning that the thermal diffusion is stronger than the diffusion of momentum. Thus, the thermal boundary layer becomes thicker than the velocity boundary layer. If c represents concentration of a tracer Γ represents the molecular diffusivity and ν/Γ the Schmidt number, Sc.

The heat flux per unit area towards the wall (q_w'') can be expressed by Fourier's law of heat conduction as

$$q''_w = -k \left(\frac{\partial T}{\partial y} \right)_{y=0}, \tag{3.33}$$

where k is the thermal conductivity and $\partial T/\partial y$ is the wall-normal derivative of the temperature. The thermal conductivity is a property of the wall material. The minus sign indicates that heat is transferred in the opposite direction of the temperature gradient. Fourier's law is probably most known for describing conduction of heat in solid materials but is relevant since at $y = 0$ there is no fluid motion and, thus, heat transfer is solely due to conduction. The heat flux can also be expressed in terms of Newton's law of cooling as

$$q'' = h(T_w - T_0), \tag{3.34}$$

where h is the convection heat transfer coefficient, T_w is the wall temperature and T_0 the fluid temperature outside the thermal boundary layer. In case of the impinging jet T_0 represents the temperature at the velocity inlet (also denoted by C_0). Note that $(T_0 - T_w)$ is constant. The convection heat transfer coefficient depends on conditions within the boundary layer and does thus change over the wall. From equation (3.33) and equation (3.34) one can formulate an expression on h as

$$h = -\frac{k}{T_w - T_0} \left(\frac{\partial T}{\partial y} \right)_{y=0}. \tag{3.35}$$

The wall heat transfer can be reformulated into a non-dimensional number, known as the Nusselt number, according to

$$Nu = \frac{hL}{k} = -\frac{L}{T_w - T_0} \left(\frac{\partial T}{\partial y} \right)_{y=0}, \tag{3.36}$$

where L defines some characteristic length-scale. For the impinging jet it is represented by D_0. As seen from the scaling Nu is proportional to the dimensionless wall-normal temperature gradient at the surface. The Nusselt number defines the ratio of convection heat transfer to conductive heat transfer between the wall and the moving fluid. In case of forced convection the space averaged Nusselt number depends on the Reynolds number and the Prandtl number whereas the local Nusselt number depends also on some spatial variable. Under specific conditions (no pressure gradient and $Pr = 1$) the heat and momentum transfer can be related according to Reynolds analogy as

$$Nu = \frac{1}{2} C_f Re Pr. \tag{3.37}$$

In most situations the Prandtl number does not equal unity why modified versions of the Reynolds analogy have been defined. As will be seen from the results presented in this thesis the instantaneous Nusselt number shows momentarily and locally the same trend as the instantaneous friction coefficient, i.e. $Nu \propto C_f$. Under these circumstances Reynolds analogy is believed to be of relevance.

CHAPTER 4

Turbulence modeling

4.1. Introduction

In principle, the complete system of governing equations (conservation of mass, momentum and energy) can be solved numerically for all parameter values. However, for large Reynolds numbers the smallest scales of the problem become so small that no one has the computer resources to obtain a fully resolved flow field. Also, for any practical problem one is not interested in instantaneous data of the flow, which are random, but rather in quantities that are reproducible (i.e. deterministic). Thus, one has to reduce the amount of data in such a way that the reduced problem (equations) have deterministic solutions. This reduction can be achieved in several ways. For example by averaging, i.e. ensemble-, spatial- and/or temporal-averages. In the latter case, one eliminates time dependency altogether, which leads to an averaged stationary problem. This approach is reasonable for statistically stationary flows. However, for flows that contain unsteady coherent structures, this approach may lead to loss of essential information.

Within the framework of the Reynolds Averaged Navier-Stokes (RANS) one often assumes that the flow is statistically stationary (or close to that state). The averaging within RANS eliminates the details of turbulence in both space and time. Due to the nonlinearity of the Navier-Stokes equations additional terms, the Reynolds stresses ($\overline{u_i' u_j'}$), appear in the averaged equations. These terms are the origin to the so-called closure problem. Thus, to solve the RANS equations, one has to express the unknown correlations in terms of the known (averaged) dependent variables. Such expressions lead to the formulation of turbulence models.

Probably the most well known model is the so-called $k-\varepsilon$ model in which the turbulent scales are determined from two transport equations, i.e. the transport equation for the turbulent kinetic energy k and the transport equation for the dissipation rate of turbulent kinetic energy ε. The turbulent length-scale can thus be defined as $k^{3/2}/\varepsilon$, the turbulent velocity-scale as $k^{1/2}$ and the turbulent time-scale as k/ε. The basic two-equation model is the so-called standard $k-\varepsilon$ model. There are however more sophisticated models developed, such as the realizable $k-\varepsilon$ model and the renormalization group $k-\varepsilon$

model (RNG). The turbulent scales can also be obtained by solving alternative transport equations as in case of e.g. the $k-\omega$ model.

The basic philosophy for this category of models is to describe the turbulent momentum transfer by an additional viscosity term, the so-called eddy viscosity ν_t. In analogy to equation (3.8) the turbulent-viscosity hypothesis (Boussinesq hypothesis) relates the Reynolds stresses to the mean velocity gradients as

$$\overline{u_i' u_j'} = \frac{2}{3} k \delta_{ij} - 2\nu_t S_{ij}, \tag{4.1}$$

where ν_t, for the standard $k-\varepsilon$ model, is given by

$$\nu_t = C_\mu \frac{k^2}{\varepsilon}. \tag{4.2}$$

In the above equation C_μ is a positive model constant, determined from experimental data. The advantages with this approach is its simplicity and the relatively low computational cost that is associated to the computation of ν_t. The main disadvantages of the turbulent-viscosity hypothesis are related to isotropy and linearity of the model. The model assumes that the anisotropy tensor ($a_{ij} = \overline{u_i' u_j'} - \frac{2}{3} k \delta_{ij}$) is aligned with the mean rate of strain tensor S_{ij}. This alignment, however, is not present even for simple shear flows. The insensitivity to rotation is another weakness of the Boussinesq approach. Thus, flows featuring strong mean streamline curvature or rotation are not possible to accurately predict. Furthermore, history effects can not be accounted for, which may cause nonphysical behavior. In the $k-\varepsilon$ model the production of turbulent kinetic energy $\mathcal{P}_k$ is expressed in terms of the scalar quantity ν_t and is given by $\mathcal{P}_k = 2\nu_t S_{ij}^2$. As seen, the production cannot be negative which may cause excessive level of turbulence in, for instance, stagnation flows (such as the impinging jet).

There are models, within the RANS context, that do not feature the above discussed deficiencies. An example of such a model is the Reynolds Stress Model (RSM). In this model the production is not modeled but directly given by equation 3.30, why the rotational part of the mean flow is accounted for. Furthermore, this model does not use the linear Boussinesq hypothesis. Instead, transport equations are solved for the individual Reynolds stresses. The computational cost and complexity of this model is, however, significantly higher relative to the eddy viscosity models.

4.2. Large eddy simulation

To fully describe a turbulent flow, all scales of motion, from the largest energetic scales ℓ_0 to the smallest Kolmogorov scales η, must be resolved. The relation

between these two scales is for isotropic turbulence described by $\frac{\ell_0}{\eta} = \mathcal{O}(Re^{3/4})$. In three dimensions the number of degrees of freedom becomes $\mathcal{O}(Re^{9/4})$. The shortest characteristic time-scale is represented by the time it takes for information to be advected through the smallest eddy, i.e. η/u_0. This time-scale is also of $\mathcal{O}(Re^{3/4})$. Thus, the computational requirement for DNS (Direct Numerical Simulation), resolving all the scales of the Navier-Stokes equations, behaves as $\mathcal{O}(Re^3)$. Therefore, DNS cannot be applied to complex geometries and higher Re flows.

If one is interested in the dynamics of the flow and/or when the RANS framework is inadequate (lack of general models and lack of well calibrated relations) one may use Large Eddy Simulation (LES). In LES one introduces spatial averaging, i.e. filtering. The filtering is aimed at eliminating or smoothing out fluctuations smaller than the predefined cutoff wavenumber. This wavenumber is in many cases equal or proportional to the grid size. The spatial filtering of the Navier-Stokes equations introduces, similar to the averaging within RANS, a new group of terms. These terms are referred to as the Sub-Grid-Scale (SGS) terms or the Sub-Filter-Scale (SFS) terms and have to be modeled, by a so-called SGS model, in order to close the system of equations. Under certain conditions, they can also be ignored, which leads to a reasonable approximation if the grid is fine enough. In contrast, one cannot neglect the Reynolds stresses. This is so since the size of the SGS terms can be made, theoretically, as small as one wishes (depending only on the filter size). In contrast the Reynolds stresses, though are second order in terms of the fluctuations, cannot be reduced to arbitrarily small values, but remain finite and balance some other terms in the RANS equations.

In LES the larger eddies are explicitly computed and one accounts for the effects of the unresolved small scales on the resolved ones through the SGS model. In this model approximations to the SGS terms are sought. For the SGS model to be generally valid one must have high enough grid resolution in order to resolve the problem dependent scales. This corresponds to the unresolved scales being problem independent, i.e. of an universal character. On average, such behavior is found in the inertial subrange of the turbulent kinetic energy spectrum. In true LES one uses explicit filtering and explicit SGS modeling. Several models have been developed during the past years. The first model was derived by Smagorinsky (1963), the so-called Smagorinsky model. This is a simple model and has been the foundation for many of the later developed ones. (For detailed information on the complete subject of LES see e.g. Sagaut (2001).)

4.2.1. *Filtering*

In order to reduce the number of degrees of freedom, and thus also the computational cost, a spatial low-pass filter is applied to the dependent variables.

However, when doing this one trades accuracy for performance since the amount of information contained in the variables decreases with increasing filter width. Thus, one must find an applicable balance between these two aspects. This can be done properly only by *a posteriori* analysis. The filtering operator is assumed to be linear, distributive and commutative with respect to derivative operators. One often adds further constrains on the filtering process. For example, one often requires that the filtering process is invariant under uniform translation (Galilean invariant). Another constrain may be that the averaging process satisfies the above mentioned properties also at the discrete level. Additional constrains may be related to preserving certain integral quantities, such as energy. It is not self-evident that these constraints are necessary conditions for a physical solution. It is rather assumed that these constraints are sufficient. However, if the SGS terms do behave as indicated above, i.e. vanish as the filter width approaches zero, then the error due to the constraints should also vanish. (Unless the two branches of solutions are disconnected and the result depends on the path of approach to the solution, i.e. multiple solutions in the extended parameter space that includes the filter size. There is however no evidence for any such behavior.)

A general explicit spatial filter can in physical space be defined as

$$\overline{\mathbf{u}}(\mathbf{x}) = G \star \mathbf{u} = \int_{-\infty}^{\infty} G(\mathbf{x} - \xi)\mathbf{u}(\xi)d\xi, \tag{4.3}$$

where $\overline{\mathbf{u}}$ is the space filtered velocity (not to be confused with the averaging within RANS), G is the filter kernel and $G \star \mathbf{u}$ is the convolution of G and $\mathbf{u}$. The filter function for the commonly applied top-hat filter can, in 1-D, be written as

$$G(x - \xi) = \begin{cases} \frac{1}{\Delta} & \text{if } |x - \xi| \leq \frac{\Delta}{2} \\ 0 & \text{otherwise} \end{cases}, \tag{4.4}$$

where Δ is the filter width or filter size. By taking the Fourier transform of the kernel one obtains the so-called transfer function $\widehat{G}$. This function is non-local in spectral space for the top-hat filter, i.e. there is not a distinct separation of frequencies. On the contrary, a filter function that is local in spectral space, i.e. the sharp cutoff filter, is non-local in physical space. Note that the spatial filtering implicitly introduces temporal filtering since the smallest resolved time-scale can be associated to the size of the smallest resolved length-scale (see Sagaut 2001, pp. 13).

The linear nature of the filter does not commute with the nonlinear advection term why an extra stress term is, as shown below, introduced. After applying a general filter, the momentum equations (3.3) become

$$\frac{\partial \overline{u}_i}{\partial t} + \frac{\partial}{\partial x_j}(\overline{u_i u}_j) = -\frac{\partial \overline{p}}{\partial x_i} + \frac{1}{Re}\frac{\partial}{\partial x_j}\frac{\partial \overline{u}_i}{\partial x_j}. \tag{4.5}$$

In this form the system of equations are not closed. To solve this the nonlinear term can be expressed by using Leonard decomposition as

$$\overline{u_i u}_j = \overline{u}_i \overline{u}_j + \tau_{ij}, \tag{4.6}$$

where τ_{ij} is the so-called SGS stress tensor (the SGS terms). If one expands the unfiltered variable in terms of the filter size, one can show that the SGS stress is second order in the filter size. With the above defined decomposition the momentum equations takes the following form

$$\frac{\partial \overline{u}_i}{\partial t} + \frac{\partial}{\partial x_j}(\overline{u}_i \overline{u}_j) = -\frac{\partial \overline{p}}{\partial x_i} + \frac{1}{Re}\frac{\partial}{\partial x_j}\frac{\partial \overline{u}_i}{\partial x_j} - \frac{\partial \tau_{ij}}{\partial x_j}. \tag{4.7}$$

As the solutions to the problems presented herein are smooth and do not contain discontinuities or shocks the nonconservative form of the momentum equations can be used without affecting the accuracy. By dropping the overbars the momentum equations can in their final form be written as

$$\frac{\partial u_i}{\partial t} + u_j \frac{\partial u_i}{\partial x_j} = -\frac{\partial p}{\partial x_i} + \frac{1}{Re}\frac{\partial}{\partial x_j}\frac{\partial u_i}{\partial x_j} - \frac{\partial \tau_{ij}}{\partial x_j}. \tag{4.8}$$

In equation (4.8) the convective term is written in advective form as compared to the divergence form in equation (4.7). It should be pointed out that for any solution of the governing equations, the conservative and non-conservative forms are identical. The differences between the two formulations arise only for the discrete formulations and corresponding solutions. The divergence form is conservative *a priori*, also from a numerical perspective.

The role of the SGS terms is, as mentioned above, to account for the effects of the unresolved scales on the resolved ones. If the filter size is much larger than the Kolmogorov scale the smallest resolved scales become large and molecular viscosity cannot account for dissipation. Energy build-up among the smallest scales must hence be handled by the SGS terms. A second role of the SGS terms is to allow energy transfer from the small scales to the larger ones, i.e. backscatter. The former property is a mandatory property of SGS models. The second property is often mentioned as being an important property.

Backscatter is important in simulations of e.g. transition, in which growth of disturbances is to be determined.

In LES one may use an explicit or an implicit filter as long as they account for the properties of the SGS terms. As the grid is refined there is one basic difference between these two approaches. With explicit filtering the solution approaches that of the filtered governing equations whereas for implicit filtering the solution approaches that for DNS. One example of an implicit filter is any local averaging operator or any local polynomial approximation to the dependent variable. An often used implicit filter is the discretization scheme (based on finite differences, finite volumes or finite elements). Explicit filtering has the advantage that it clearly separates two important parameters. Namely, the filter size, which is related to the physics of the flow, and the grid size, which is related only to the resolution of the small scales. The ratio between these two parameters must be chosen with care. The ratio can be made smaller for high order schemes as compared to low order schemes. In the work by Chow & Moin (2003) the minimum ratio for the fourth order scheme was concluded to be twice the cell size and for the second order scheme it was concluded to be four times the cell size. This in order not to mask the contribution from the unresolved terms.

The uniform filter (constant filter width) is of convolution type and does commute with partial derivatives whereas a nonuniform filter features variable filter width and does not commute with partial derivatives. A consequence of this is that commutators, i.e. commutation errors, are introduced into the solution. The commutator terms may be handled by the SGS model but this adds of course additional complexity to the modeling. As stated by Chow & Moin (2003) a fourth order explicit filter should be used in order to separate the commutation errors from the modeled terms, which are of second order. Applying explicit filtering is associated with complications on inhomogeneous or unstructured grids. Using a simple filter in such cases introduces additional errors as the form of the filtered LES equations deviate from that of the Navier-Stokes equations. There are however filtering methods that allow variable grid spacing (see e.g. Vasilyev *et al.* 1998; Marsden *et al.* 2002). More details on homogeneous filtering can be found in the work by e.g. Sarghini *et al.* (1999), Gullbrand (2002), Gullbrand & Chow (2002), and Gullbrand & Chow (2003).

Detailed studies of the influence from filtering in practical low order LES was conducted by Brandt (2004). He showed that explicit filtering of the whole velocity field is not possible on a "normal" resolution LES grid. The background to this is that as the filter width was increased the SGS terms grew slowly and finally, as a consequence of too low effective grid resolution, diminished. Instead, if only the nonlinear terms were filtered the desired behavior was obtained, i.e. the numerical error diminished while the SGS terms grew. Clear separation was obtained at a filter width of two. As stated by Lund (2003) the filtering of the nonlinear terms is the critical and thus the essential issue in

nonuniform simulations. Thus, for consistency explicit filtering of the nonlinear terms should be performed at each time step.

Relative to explicit filtering, implicit filtering is less computationally expensive and does not involve commutation errors (cf. Fureby & Grinstein 2002). Implicit filtering has some drawbacks though. Firstly, as the cutoff wavenumber is determined by the grid spacing and the filter does not have a sharp cutoff in the Fourier space, the smallest resolved scales are often influenced by numerical errors. Thus, high order discretization schemes and high grid resolution are essential in order to minimize the contribution from these errors. Secondly, the influence from the implicit model, i.e. the discretization scheme itself, is difficult to assess. When comparing different SGS models explicit filtering is more appropriate as it is independent of the grid spacing. The filtering process and the SGS modeling must be considered as an inseparable issue since the filtering operator may be more suited for a *model A* than for a *model B* (see Stefano & Vasilyev 2002). This issue is of great importance for models relying on information contained in the smallest resolved scales. Stefano & Vasilyev (2002) studied the influence from sharp (cutoff) and smooth (top-hat and Gaussian) filters. They found that the SGS stress tensor and the spectral content of the solution depends strongly on the applied filter. In order to construct efficient SGS models a sharp cutoff filter should be used as this filter yields a distinct separation of scales. Furthermore, the cutoff filter is Galilean invariant. In top-hat and Gaussian filtering the limit between resolved and modeled scales is not well defined and the modeling process becomes significantly more complicated. However, the sharp cutoff filter cannot be applied in bounded domains as it is non-local in physical space. This is why top-hat filters are commonly used in complex geometries.

Despite the known theoretical advantages of explicit filtering the practical benefits are, as stated by e.g. Gullbrand & Chow (2002), hard to motivate. Furthermore, as shown in the work by Lund (2003) the accuracy of their LES simulations was improved at a greater rate with implicit filtering and mesh refinement as compared to explicit filtering. Due to the limitations in computer hardware and the complexities involved in inhomogeneous filtering, implicit filtering is most frequently used in LES. As stated above, mesh refinement of the grid results in less influence from numerical errors on the smallest resolved scales. This in conjunction with the additional complexity of inhomogeneous explicit filtering is the motivation behind applying the "universal" implicit filtering approach within this work. The shape of the implicit filter cannot be determined. However, since we (and practically the whole LES community) do not apply the filtering on the boundary conditions, it never enters explicitly in the equations and thereby its explicit form is not required at all.

4.2.2. *SGS modeling*

The SGS stress tensor has to be modeled in order to close the system of equations. As stated above, these terms may also be ignored provided that the grid spacing is fine enough. The first explicit SGS model was developed in the sixties by Smagorinsky (1963). In this model the SGS stress tensor is related to the filtered rate of strain, in analogy to eddy viscosity models in RANS. The introduced eddy viscosity is modeled by using the filter (grid) size as the reference length-scale. One drawback with this model is that the model constant, C_s, is not universal but case dependent if the grid is not fine enough. In addition the model cannot handle backscatter, i.e. it is absolutely dissipative as the rate of energy transfer to the modeled scales is strictly positive.

The Smagorinsky model has clear problems in near-wall regions where damping or wall functions are required. During the years a large number of improved models have been developed. The dynamic model by Germano *et al.* (1991) allows local values of the model coefficient, C. The model coefficient is calculated from the resolved motion and approaches zero in regions of fully resolved flow, i.e. the effects of the model diminish. This model is based on two filter functions. The first one is most commonly represented by the grid size and the second one is a so-called test filter. The test filter is the larger, often chosen to be around twice the grid size, and used for calculating C. A potential problem with this model is that the model coefficient can become indeterminate as it may change sign in the flow field. This can lead to numerical instability. To solve the problem the model coefficient can be bounded. Artificial limiting of C was worked on by Olsson & Fuchs (1996, 1998). Note that a negative value of C (however bounded) is not a completely undesired feature as it allows the dynamic model to account for backscatter.

As the coefficient in the dynamic model is a scalar quantity the model becomes isotropic. This means that the smallest scales, at test filter level, are assumed to be of universal character. In some cases it is difficult to assess an overall universality of the smallest resolved scales. In the Divergence Dynamic Model (DDM), derived by Held & Fuchs (1997), C is divided into three parts, one in each spatial direction. Hence, sub-grid anisotropy could be handled in a more correct manner. This model is based on the fact that only the divergence of the SGS stress tensor is used in the momentum equations. In the scale similarity model (SSM) (see Bardina *et al.* 1980) it is assumed that the interaction between resolved and modeled scales behaves similar for different filter sizes. This model has a major drawback as it is not dissipative. This problem was solved by Bardina *et al.* (1983) who proposed an *ad hoc* approach by introducing the so-called mixed model. The mixed model is a combination of SSM and the Smagorinsky models.

In the work by Tammerman (2003) it was shown that for calculation of separated channel flow the grid resolution and the near-wall treatment were of

major importance whereas the choice of SGS model was more or less nonessential. Hence, for their specific problem a simple model in conjunction with a fine mesh provided accurate results. As stated by Geurts (2003) a sophisticated SGS model at fairly large filter width produces similar results to a poor model at small filter width. Depending on the type of results wanted and on the complexity of the flow and geometry simple models may provide satisfactory results (see also da Silva & Pereira 2004).

From the behavior of SGS models and the construction of SSM one may conclude that it is roughly equivalent using an explicit model as using a finer grid without an explicit SGS model. In some cases using an explicit model may pay-off computationally. Whereas in other cases, not using an explicit model can be compensated for by refining the grid. In the computations presented in this thesis we have not considered explicit SGS modeling. Instead we have prioritized the grid resolution. However, the error introduced by neglecting the SGS terms and instead introducing artificial dissipation is most probably not more harmful than applying an improper explicit model incapable of handling complex flow features such as dissipation, anisotropy and backscatter. The computational resources saved by considering implicit modeling may, roughly, permit construction of a grid with twice as many cells.

In the work by Fureby & Grinstein (2002) an implicit model was used for computation of high Re compressible flows. For compressible flow the implicit method is referred to as the MILES (Monotone Implicit LES) approach. They stated that an explicit SGS model capable of handling inhomogeneities and rapid deformation becomes far too complex to be of practical interest. This fact motivated them to use a nonconventional implicit approach. Their results showed that the implicit method predicted the energy cascade and statistical moments, for free jets and wall-bounded flows, better than the eddy viscosity models and comparable to the anisotropic differential stress model (DSM). However, the computational effort using the DSM model was 68% higher as compared to the implicit model. An implicit modeling approach was also used in the work by Margolin *et al.* (1999). It produced similar results as an explicit eddy-viscosity model. They concluded that the solvers implicit viscosity served well as an effective SGS model and that second order accuracy was needed in order not to obtain excessive dissipation. Too high dissipation resulted in steeper energy spectrum within the inertial subrange and hence also in slightly lower variance.

Pasquetti (2005) performed LES with and without SGS modeling of turbulent wake flow (however in a spectral manner). From the results they concluded that the no-model approach yielded comparable or even better results, regarding first order statistics and spectral content, than the explicit approach. In the work by Meinke *et al.* (2002) turbulent flows were studied by means of different types of SGS models, grid resolutions and numerical schemes (second order mixed central-upwind scheme and sixth order compact schemes). The

results showed that using an explicit SGS model does not improve the quality of the solution. This regardless of the Reynolds number, grid resolution and numerical scheme. More important for the results are the mesh resolution and the filtering parameters.

Detailed studies on the present code with and without explicit modeling have been conducted by Olsson (1997) and Olsson & Fuchs (1996, 1998). In their later work (cf. Olsson & Fuchs 1998) they studied the SGS model effect for an impinging jet at $Re_D = 10^4$ and with a nozzle-to-plate spacing of four jet diameters. The numerical scheme was the same as within this work. The reference case was a highly resolved implicit simulation (128^3 cells on the highest multi-grid level). Two explicit models were considered, the dynamic Smagorinsky model and the stress-similarity model. Their conclusion was that the implicit method yielded results of same quality as the explicit approaches and, furthermore, the effect from the SGS models were not masked by the numerical scheme.

4.3. Near-wall treatment

The near-wall region is of great importance for turbulent flows since within this region viscous effects are important. In high Reynolds number wall flows the grid size and consequently the smallest resolvable scales can be magnitudes larger than the physical scales of the near-wall flow. The physical scales must hence be treated by some sort of model, often termed as "wall function". This kind of modeling is, as stated by Pope (2000), of limited generality in complex flows such as flows with e.g. separation and impingement. As depicted in the work on separated channel flow by Tammerman (2003) the results were sensitive to the type of the implemented wall-law. The shown discrepancies originated from the basic problem of predicting correct instantaneous wall shear stress.

The most common approach, which also is applied within this work, is to resolve the flow in a similar manner as in DNS, i.e. by using wall-normal grid stretching. This is referred to as Quasi-Direct Numerical Simulation by Spalart (2000) since all eddies in the boundary layer are resolved and the SGS stresses are of the same order of magnitude as the viscous stresses. However, the required grid spacing significantly affects the computational cost and is thus difficult to actualize in complex geometries. By using wall boundary treatment the computational time can be reduced by a factor of 10 as shown in the work on trailing edge flow by Wang (1999). Therefore improved SGS modeling for the near-wall region of complex flows is desirable.

Due to the amount of computer resources needed to resolve the near-wall region alternative approaches have been developed that also involve unsteady RANS. The near-wall RANS simulation is matched to the outer LES simulation at some deterministic distance from the wall. One of these approaches is the, so-called, Detached Eddy Simulation (DES) technique developed by Spalart *et al.* (1997). In this method the Spalart-Allmaras one-equation turbulence model is

employed. Another approach, implemented by Davidson & Peng (2003), is the so-called hybrid LES-RANS method. In this method a two-equation k-ω model is used in the near-wall region. One problem with these kind of approaches is to obtain appropriate matching between the two different simulation strategies, e.g. where the interface shall be located, how to determine it and how to assess correct boundary conditions for the LES (spectral content, time and space correlations).

In-spite of the efforts to develop a general treatment of solid walls, it is clear that so far there exist no generally valid models. One may also argue that there is only little hope for such models, unless they include local and non-local information, making such modeling dependent on the specific problem (i.e. not general).

4.4. Modeling of scalar transport

The spatial filtering of the scalar transport equation (3.32) yields an additional term that accounts for the sub-grid-scale fluxes on the resolved scalar concentration. The filtered scalar equation is

$$\frac{\partial \overline{c}}{\partial t} + \overline{u}_j \frac{\partial \overline{c}}{\partial x_j} = \Gamma \frac{\partial}{\partial x_j} \frac{\partial \overline{c}}{\partial x_j} - \frac{\partial \psi_j}{\partial x_j}. \tag{4.9}$$

The additional term ψ_j is the scalar SGS (of the turbulent fluxes) and can be treated by models in analogy to the momentum SGS terms. As in case of momentum SGS, for adequately fine spatial resolution one may neglect altogether the explicit scalar SGS terms. For further information on scalar SGS modeling see e.g. Revstedt (1999).

CHAPTER 5

Numerical aspects

As a complement or as a replacement to experimental work on fluid dynamics digital computers can be used to numerically solve the Navier-Stokes equations. The different methods solving these equations are tools that are used in Computational Fluid Dynamics (CFD). The problem under consideration may either be steady-state or time-dependent. The numerical methods must fulfil some well-known properties, namely: *consistency*, *stability* and *convergence*. *Consistency* implies that the discrete problem is an approximation to the differential one. A solution method is *stable* if any given error remains bounded (in certain sense) during the solution procedure. Stability may be investigated by different methods, including the linear normal-mode analysis (von Neumann). *Convergence* implies that as the grid is refined the solution to the discrete problem approaches the solution to the differential problem. According to Lax equivalence theorem (see Tannehill *et al.* 1997), which is valid for certain linear initial value problems, the following relation holds: *consistency* + *stability* <=> *convergence*. Naturally, the problem to be solved has to be *well-posed*. Well-posedness implies that a solution to the problem must exist and be unique, and depend continuously upon the initial and boundary data.

For the results presented within this work an in-house developed code has been employed. This code is constructed on a staggered Cartesian grid and for the discretization of the governing equations finite differences have been used. On structured grids finite differences allow easy implementation and are computationally highly efficient. One potential drawback when compared to the finite volume approach is that high-order finite difference methods, applied to the continuity equation, may not be inherently conservative. However, this is not the case here.

5.1. Partial differential equations

When solving physical problems governed by partial differential equations it is important to be familiar with the basic mathematical properties of the system of equations. This in order to formulate appropriate numerical schemes and boundary conditions. The classification can be performed by analyzing the symbol of the principle part of the system. There are four main categories of

partial differential equations: the hyperbolic, the parabolic, the elliptic and all the others not belonging to any of these categories. Different assumptions made on the Navier-Stokes equations may lead to systems of different types. The character of the systems indicates the character of the flows (wave-dominated, diffusion dominated or evolutionary, which are hyperbolic, elliptic and parabolic, respectively).

Hyperbolic equations characterize wave propagation problems, i.e. the solution depends solely on conditions at certain parts of the domain (so-called "domain of dependence"). This is also the case for parabolic equations for which the domain of dependence is the limiting case and it extends to the whole domain. Parabolic equations involve dissipative effects, which smooth out sharp gradients, whereas hyperbolic equations do not involve any dissipative effects, i.e. discontinuities may occur.

For hyperbolic and parabolic equations all characteristics are real. An elliptic system has no real characteristics at all. The number of ingoing characteristics determines the number of required boundary conditions. For elliptic systems, which are always of even order, $2m$, one has to specify m conditions on all boundary points. The incompressible, steady-state, Navier-Stokes equations are of order $2d$, where d is the dimension of the problem. Thus, one has to specify d conditions on all boundary points. These conditions may be of different types, i.e. one may specify the velocity vector on some of the boundaries and possible some other forms of conditions at other boundaries. When the velocity vector is specified, global mass conservation has to be satisfied. The time dependent incompressible Navier-Stokes equations do not belong to any of the three categories; they are, so-called, incompletely parabolic. The system requires boundary conditions as an elliptic system (i.e. d conditions on all boundary points at all times) and additionally, initial conditions at all other points of the domain under consideration.

5.2. Spatial discretization

One of the major problems in numerical simulation of fluid flow are the errors introduced by the spatial disctretization. These errors are primarily due to the finite size of the grid. However the choice of discretization scheme, i.e. truncation error and characteristic behavior (dispersive or dissipative), is of course also of great importance for the outcome of the simulation. There is a general belief that higher order numerical accuracy is important for handling the physics of the small scales that are supported on a given grid. This, however, is highly dependent on the scheme itself and not only on its formal order of accuracy. High order schemes and high grid resolution have a stronger tendency to cause nonphysical oscillation and slow convergence rate as compared to low order schemes and coarse grids.

Discrete spatial derivatives can be derived from Taylor-series expansion. The Taylor series for a continuous function $u(x)$ in the vicinity of x_i can be written as

$$u(x) = u(x_i) + \sum_{n=1}^{N} \frac{(x - x_i)^n}{n!} \left(\frac{\partial^n u}{\partial x^n} \right)_i , \tag{5.1}$$

where N defines the highest order term. Rewritten as an expression for the first order derivative at x_i the following is achieved

$$\left(\frac{\partial u}{\partial x} \right)_i = \frac{1}{(x - x_i)} \left[u(x) - u(x_i) - \sum_{n=2}^{N} \frac{(x - x_i)^n}{n!} \left(\frac{\partial^n u}{\partial x^n} \right)_i \right]. \tag{5.2}$$

By replacing x by x_{i+1} or x_{i-1} forward or backward differencing is obtained and by combining these two central differencing is obtained. The value of the approximated derivative may differ significantly between these three methods. However, this difference decreases as the grid is refined.

The forward difference scheme can, if truncated, be written as

$$\left(\frac{\partial u}{\partial x} \right)_i = \frac{u_{i+1} - u_i}{x_{i+1} - x_i} - \frac{x_{i+1} - x_i}{2} \left(\frac{\partial^2 u}{\partial x^2} \right)_i - \frac{(x_{i+1} - x_i)^2}{6} \left(\frac{\partial^3 u}{\partial x^3} \right)_i . \tag{5.3}$$

The leading error term, i.e. the second term on the right hand side, is directly proportional to the grid spacing, meaning that the approximation is of first order accuracy. The second term is also proportional to the second derivative of u. The consequence of this is that the scheme is dissipative in nature. There is also some dispersion introduced by the third term. But as this term is proportional to the square of the grid spacing the error due to dispersion is low. Thus, the forward and backward schemes, i.e. upwinding, is of a dissipative character.

The central difference scheme can, when truncated, be written as

$$\begin{aligned} \left(\frac{\partial u}{\partial x} \right)_i = \frac{u_{i+1} - u_{i-1}}{x_{i+1} - x_{i-1}} - \frac{(x_{i+1} - x_i)^2 - (x_i - x_{i-1})^2}{2(x_{i+1} - x_{i-1})} \left(\frac{\partial^2 u}{\partial x^2} \right)_i \\ - \frac{(x_{i+1} - x_i)^3 + (x_i - x_{i-1})^3}{6(x_{i+1} - x_{i-1})} \left(\frac{\partial^3 u}{\partial x^3} \right)_i . \end{aligned} \tag{5.4}$$

Also here the leading error term is directly proportional to the grid spacing and the second derivative of u. However, for uniform grids this term vanishes

and the central scheme becomes second order accurate. Thus, intuitively, in order to maintain accuracy the grid should be as uniform as possible. But as the truncation error also depends on derivatives of u minimum error is, for a given number of grid nodes, obtained on stretched grids. Regions featuring steep gradients, such as boundary layers, demand high resolution in order to resolve the local physical scales and to minimize the error. (In order not to alter the formal order of accuracy one can use coordinate transformation, i.e. construction of an uniform computational grid by transforming the governing equations by analytically derived metric coefficients, see section 5.5.)

By increasing the formal order of accuracy the magnitude of the leading error term decreases, resulting in less dissipative or dispersive effects. This is of great importance for time dependent flows containing small scale structures, since too high artificial dissipation will weaken or even prevent the development of these structures and thus influence the reliability of the simulation. However, applying a high order method on a coarse grid incapable of resolving important scales is not desirable. A high order method relies on information from a greater number of neighboring nodes as compared to low order methods. Thus, a high order method acts as a filter, smoothing out the smallest resolvable scales. If the grid is coarse this results in inaccurate representation of steep gradients. The advantages of high order methods can only be gained on relatively fine grids. If the grid is fine enough is, as stated by Ferziger & Peric (2001), both problem and method dependent and cannot be determined *a priori*. One should note that the order of the truncation error does not provide any information about the magnitude of the error only how the error changes as the grid is refined.

A less common use of larger number of grid data to express derivatives is not for attaining higher order but rather to improve the high frequency properties of a numerical scheme. In recent years one has developed discretization schemes that have better dissipative and dispersive properties for a wider range of scales (wave-numbers). Since these schemes are of lower order, the additional data is used to "optimize" the above mentioned properties. These optimal schemes may be useful when explicit filtering is used. Another recent trend in higher order schemes, is using compact versions. These version involve less number of grid points as compared to classical higher order schemes, but on the other hand they do require derivatives of the dependent variables,

The choice of method for discretization of the governing equations is non-trivial and must be based on the complete problem. In the present work no explicit SGS model is used and hence the discretization scheme must be designed with this in mind. Furthermore, to avoid masking of the SGS stress by the truncation error high order schemes are needed. For the spatial discretization of the advection term in the momentum equation (4.8) a $\mathcal{O}(h^3)$ upwind-biased scheme, proposed by Rai & Moin (1991), has been used. Originally this scheme was used for DNS simulations of fully developed channel

flow. In DNS the numerical dissipation should be minimized since the dissipation of energy is fully handled by the action of viscosity. Rai & Moin (1991) used this weakly dissipative scheme in order to control aliasing errors and, to minimize the dissipation, an extra fine mesh was constructed. (As verified by Olsson (1997), Olsson & Fuchs (1998) and Revstedt (1999) the considered discretization of the advection term adds appropriate amount of dissipation to the simulation to allow implicit SGS modeling.) Applied to the advection term the finite difference equation can be written as

$$FDE_{adv} = u_{i,\,j}\frac{2u_{i+1\,,j} \pm 3u_{i,\,j} \mp 6u_{i-1,\,j} \pm u_{i-2,\,j}}{6h}, \tag{5.5}$$

where h is the grid spacing. The upper operator of $(\pm)$ is used for $u_{i,\,j} > 0$ and the lower for $u_{i,\,j} < 0$. An identical expression can also be constructed by introducing an explicit artificial viscosity term that is added to the standard fourth order central differences. In this way one can easily identify the size and form of the added (artificial viscosity) term

$$FDE_{adv} = PDE_{adv} - TE_{adv} = PDE_{adv} - \frac{1}{12}\,|u|\;h^3\frac{\partial^4 u}{\partial x^4} + \mathcal{O}(h^4). \tag{5.6}$$

It should be pointed out that this estimate is not valid for the highest frequency modes that are supported by the grid, since for these modes the Taylor expansion converges slowly and the leading term is not dominating over the rest of the terms in the expansion.

The other terms in the momentum and continuity equations are approximated by fourth order central differences.

5.2.1. *Scalar equation*

In the spatial discretization of the scalar equation (4.9) the $\mathcal{O}(h^3)$ upwind-biased scheme has been used for the convective term. The diffusive term is approximated by $\mathcal{O}(h^4)$ central finite differences. Near boundaries a hybrid scheme has been used for the convective term. This scheme implies that central differences are used where diffusion is dominant and upwinding where convection is dominant.

5.3. Temporal discretization and solution procedures

In LES the time step Δt should primarily be limited by the physical time limitation, based on the integral and Kolmogorov time-scales. Such limitation would imply also that the CFL number will be lower than unity. For the simulations presented herein the maximum CFL number in time and space has

been within the range of 0.2 ± 0.05. A too high value of this criterion causes the solution to explode.

The momentum equations have been advanced in time by a three-step Runge-Kutta (RK) method and, as the flow is treated as incompressible, a pressure correction technique has been used to ensure a divergence free solution. The pressure correction involves repeated solution of a Poisson equation. The Poisson equation is of an elliptic character and can be treated in an iterative manner. In this specific case a point Gauss-Seidel relaxation algorithm has been used in a multi-grid framework. A multi-grid is used in order to speed up the convergence. Once the pressure corrections are computed, the velocity field is also updated, in such a way that (a linearized version of) the residuals of the momentum equations remain unaffected when the continuity equation is being satisfied.

As stated above, the time integration of the momentum equations employs a three-step Runge-Kutta scheme. Similar scheme can be used also for the scalar transport equation. However, for high Prandtl or high Schmidt numbers this may require a smaller time step for the scalar equation. Hence, in most cases we use only a low-storage second order scheme for the scalar equation and allow several time steps in each time step used for the Navier-Stokes equations.

5.4. Boundary conditions

5.4.1. *Inflow conditions*

The outcome of a numerical simulation depends strongly, as discussed above, on the discretization scheme, the computational grid and the type of modeling. However, the solution of the Navier-Stokes equations depends also strongly on the specified boundary conditions and errors or uncertainties in these. On solid walls one often specifies no-slip conditions. These conditions are well defined and can be subjected to errors only if the wall has some porosity or unresolved surface roughness. On the other hand, specifying inflow and outflow conditions is much less obvious. In general, one may be able to specify such conditions, at best, with known uncertainty. In many other cases the error in the boundary conditions is unknown, making comparisons with experiments doubtful since no definitive conclusion can be drawn by the comparison. The benefits from having an accurate scheme, a fine grid and a sophisticated SGS model may be masked by uncertainties in boundary conditions, when comparisons are made with experimental data.

In some applications, where the inflow is laminar an assumed velocity profile may be specified. For low Re flows the effect of an error in that profile disappears at a distance that depends on the viscous dissipation. In this work, essentially, three different mean profiles have been considered: the top-hat, the weakly mollified and the strongly mollified. Characteristic for the top-hat profile is that the imposed annular shear-layer is not grid independent since

the shear-layer thickness is directly determined by the local grid resolution. In contrast, the mollified mean velocity profile features a well defined shear-layer thickness. In effect, this profile is a consistent form of the LES filtering applied to the top-hat profile.

For turbulent flows, the inlet velocity profile should contain, in addition to an accurate average velocity vector, also a fluctuating component that has a turbulent spectral behavior. In most experimental setups the turbulent flow field is not fully developed and it contains (due to too short inlet sections) non-specified secondary flow and fluctuating components. The options that one has, in terms of the fluctuating component, are to impose random perturbations of known amplitude or to alter the spectral content of these perturbations such that they resemble the one predicted by Kolmogorov's theory. Random perturbations, though not physical, are modified by the Navier-Stokes equations after a rather short distance: The high frequency components dissipate quickly and the spectral content of the perturbations approaches rapidly the spectral content of a turbulent flow. On the other hand, a random perturbation which contains all modes can also promote the modes that are naturally amplified by the flow downstream. We define the randomly perturbed inlet velocity as

$$v(r,t) = V(r) + 2A(Rand(r,t) - 1/2), \tag{5.7}$$

where V is the mean velocity, A is the amplitude of the perturbations and $Rand$ is a function providing pseudo random numbers within the interval $[0,1]$. (The abnormally high viscous forces caused by the random fluctuations can, as stated by Friedrich *et al.* (2001), be overcome by artificially increasing Re and then gradually decreasing it to the desired value. By doing this the transient time is sufficient for the fluctuating energy to be distributed among all wavenumbers.)

As an alternative to random perturbations one may use the velocity field from a precursor simulation of turbulent flow as inflow conditions. In doing so the correct correlations and spectrums are achieved in the inlet plane. The drawback, though, is the amount of storage capacity needed and the time consuming precursor simulation. This method is also relatively inflexible as an additional calculation must be performed if an alternative velocity field is wanted. Within the present work, pipe flow simulations have been conducted for the prescribed Reynolds and swirl numbers (rotating pipe). These simulations have been performed in a periodic Cartesian domain with a length of $8\pi R$, where R is the pipe radius. The number of cells in (x, y, z) were $(162, 162, 194)$ on the finest out of four multi-grid levels, where z represents the streamwise direction. At each time step the midplane (xy-plane) of the pipe was saved for future use (space correlations in x and y and time correlation in z). More detailed information on the precursor simulations can be found in Hällqvist & Fuchs (2006*b*).

There are other methods developed for emulating turbulent flow. Among others, Na & Moin (1998) used a frozen velocity field from a precursor simulation of periodic channel flow as inlet condition to the DNS of divergent channel flow. Only one instant of the channel simulation was stored. The spatial streamwise direction was converted into temporal using Taylor's hypothesis. When all temporal planes had been read the frozen velocity field was updated by randomly disturbing the Fourier coefficients. By doing this the spectral content was relatively unchanged whereas the velocity signal changed character. More sophisticated methods have been used by, among others Kondo *et al.* (1997), who generated artificial divergence free isotropic turbulence from prescribed power spectral density and cross-spectral density. Methods for synthesizing turbulence have also been studied by Klein *et al.* (2003) and Kempf *et al.* (2005).

In order to trigger specific instability modes of the system one may use sinusoidal perturbations. By doing this one adds temporal correlation to the boundary, determined by the predefined frequency or frequencies, while the correlation in space remains undefined. This methodology, here referred to as periodic forcing, can be formulated as

$$v(r,t) = V(r) + Asin(2\pi St_e t), \tag{5.8}$$

where A is the amplitude of the sinus function and St_e is the forcing or excitation frequency, here expressed in terms of a Strouhal number (fD_0/V_0). In this specific case the forcing is applied in a symmetric fashion.

5.4.2. *Wall treatment*

One of the major problems inherent in LES is to resolve the flow near walls subjected to the no-slip condition. There are no easy ways of solving this problem. Wall functions are frequently used but these are not of an universal character and may become invalid in certain regions. For example, wall functions based on the logarithmic law of the wall which is only valid for fully developed boundary layer flows. Hence, the only reliable method is to fully resolve the near-wall flow. This is computationally highly expensive, why this method is limited to moderate Reynolds numbers and simple geometries. One should however not only focus on the wall-normal resolution as the small resolved scales are generally of a three-dimensional character. Hence, one needs relatively high resolution also in the streamwise and spanwise directions. In the work by Tammerman (2003) it was shown that despite adequate near-wall resolution the streamwise resolution influenced the prediction of separated flow substantially.

To determine if the resolution is sufficient viscous units are frequently used. However, this scaling is only valid for fully developed boundary layers. Within

the stagnation region scaling originating from Hiemenz solution can be used. Comparison between these two scalings reveals that the viscous one is more demanding. In the present work viscous units, even though being a crude estimate, have been used for relative comparison of different grids.

As the grid is structured, composed by rectangular cells, the resolution in viscous units will differ when going in the radial direction along the wall. This since y^+ is based on the wall friction τ_w according to

$$y^+ = \frac{y}{\delta_v} = \frac{y}{\nu\sqrt{\frac{\rho}{\tau_w}}}, \tag{5.9}$$

where δ_v is the viscous length-scale and y the wall-normal distance. Minimum resolution is attained at the location for maximum wall friction. Note that estimation of the wall resolution on the basis of the averaged flow field can be misleading since in order to properly resolve the unsteady flow the instantaneous velocity field ought to be considered.

In the simulations presented in this thesis the velocity and temperature are both equal to zero at the impingement and confinement walls.

5.4.3. *Outflow conditions*

The outflow conditions differ significantly depending on the nozzle-to-plate spacing. If the spacing is small the complete height at the outlet features positive flow (no backflow) on average and probably also instantaneously. For larger spacing there will be backflow, both on average and temporarily. Hence, the boundary condition at the outlet must be flexible and allow a variety of flow conditions without introducing errors. The present outlet boundary is given by a hyperbolic convection equation according to Olsson & Fuchs (1998)

$$\frac{u_j^{n+1} - u_j^n}{\Delta t} + U_c \frac{u_j^n - u_{j-1}^n}{h} = 0. \tag{5.10}$$

This equation results in the following discrete expression for the convection velocity U_c at the outlet

$$U_c = -\frac{h}{\Delta t}\left(\frac{u_j^n - u_j^{n-1}}{u_j^{n-1} - u_{j-1}^{n-1}}\right), \tag{5.11}$$

based on the time discretization at $n-1$. It has been shown by Olsson & Fuchs (1998) that this type of boundary condition has negligible influence on the results in the near-impingement region for the considered width of the domain.

5.5. Computational grid

The staggered Cartesian grid is generated at the initial stage of the simulation from analytical expressions. These analytical expressions are controlled by parameters given in an input file. By using this type of grid generation one maintains high accuracy also on stretched grids. The grid control parameters determine the spatial extension, mesh density in the three separate coordinate directions, number of multi-grid levels, multi-grid type and level of grid stretching.

The stretching in the direction of the wall-normal coordinate (y-direction) is defined as

$$y(\eta) = atan\left(\frac{tan(A*B)\eta}{A}\right)/B, \tag{5.12}$$

where η is the coordinate in computational space and y is the coordinate in physical space. The stretching is determined by the parameters A and B. In the two longitudinal directions the stretching function is defined as

$$x(\xi) = z(\xi) = C\left(1 + \frac{sinh((\xi/C-1)D)}{sinh(D)}\right), \tag{5.13}$$

where ξ is the coordinate in computational space and x and z are the coordinates in physical space and C and D are stretching parameters. In order to attain constant grid spacing ($\Delta\xi$ and $\Delta\eta$) during the computation the governing equations are in a 2-D framework transformed via

$$T = \frac{\partial}{\partial X} = \left(\frac{\partial}{\partial \xi}\right)\left(\frac{\partial \xi}{\partial X}\right) + \left(\frac{\partial}{\partial \eta}\right)\left(\frac{\partial \eta}{\partial X}\right), \tag{5.14}$$

$$\frac{\partial^2}{\partial X^2} = \frac{\partial T}{\partial X} = \frac{\partial}{\partial X}\left[\left(\frac{\partial}{\partial \xi}\right)\left(\frac{\partial \xi}{\partial X}\right) + \left(\frac{\partial}{\partial \eta}\right)\left(\frac{\partial \eta}{\partial X}\right)\right], \tag{5.15}$$

where X is x or y. The metric parameters, i.e. $\partial\xi/\partial X$ etc., are exactly derived from the stretching functions. When the metric coefficients are computed numerically the stretching must, as shown by Rai & Moin (1991), be smooth in order not to alter the accuracy of the numerical scheme. We compute all stretching parameters using analytical expressions and thereby avoid reduction in the numerical accuracy.

CHAPTER 6

Computational accuracy

The different types of errors can be divided into four groups. The first is related to the accuracy of the implemented models. Some of the models are approximations, in the sense that by varying certain parameters, the errors can diminish, whereas other models are not. The latter models do not approximate the real problem, independently of how refined and detailed the computations are made. The second group of errors is of numerical character and include contributions from the finite resolution in space and time and contributions from the discrete representation of derivatives (so-called discretization errors). The third group of errors becomes significantly important if the numerical solution is not fully converged (in the sense that the discrete problem is solved only approximately). The fourth error source originates from the finite accuracy arithmetic on the computer ("round-off" errors). An additional error source is that originating from the applied boundary conditions.

6.1. Modeling errors

In complex flows or at high Re errors originating from the wavenumber cutoff being located at anisotropic scales, are introduced. By refining the grid the cutoff is moved towards higher wavenumbers and the SGS scales become, hence, more homogeneous and universal in character (only weakly affected by the boundary conditions and the large scales of the flow). Furthermore, in this wavenumber regime the energy content is negligible as compared to the energy content among the larger scales. This suggests that the SGS scales have very limited influence on the low wavenumbers. (A low energy content at cutoff is also important for minimization of aliasing errors that arise from the discrete approximation of the nonlinear terms.) Under these circumstances the SGS terms can be modeled by a simple dissipative model, such as the present implicit one. For more complex flows or for higher Re (coarser grid) a model capable of handling more complex features might be necessary (such as anisotropy).

As the discretization scheme, in this work, also represents the model the error due to modeling can not be isolated. Hence, in an *a posteriori* analysis of the results the influence from the total error is accounted for. The accuracy of the results can then be verified by comparison with experimental or DNS data. Even though the detailed behavior of the present model cannot be assessed

the good correlation with experimental data, for the results presented in this thesis, indicates that the implicit modeling approach (in conjunction with a fine grid) yields results of high physical accuracy and relevance.

6.2. Numerical errors

The order of accuracy of the numerical scheme is explicitly determined by the truncation error. Common problems with first order schemes are due to the first term of the truncation error being similar to the viscous term in the governing equations. This introduces so-called artificial viscosity, which tends to reduce all gradients (dissipative). For second order schemes a characteristic problem is the influence from the odd derivative of the truncation error, which may cause dispersion (distortion of phase relations between various waves as waves with different wavelengths travels at different speeds).

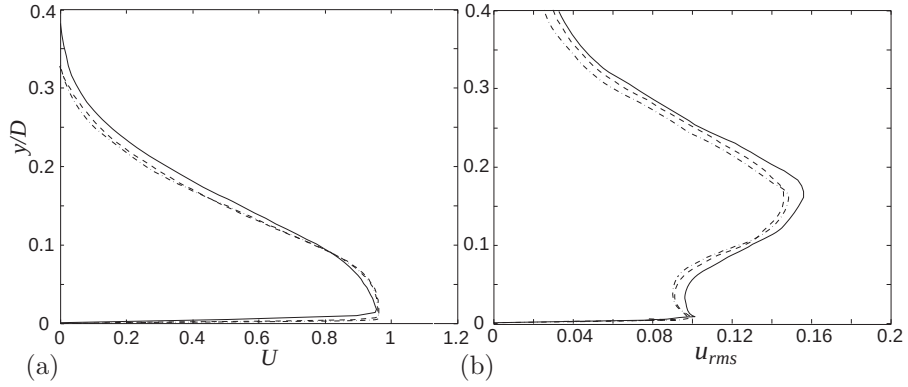

FIGURE 6.1. Influence from grid resolution on the computational results for an impinging jet with $H/D = 2$ at $Re = 20000$. Mean radial velocity U at $x/D = 1$ in (a) and u_{rms} at $x/D = 1$ in (b). (—): $194 * 98 * 194$, (- - -): $194 * 146 * 194$, (- · -): $194 * 226 * 194$.

The influence from the discretization error can be estimated from figure 6.1. Three grids with different resolution in the wall-normal direction have been considered. The coarsest grid has 98 cells in the y-direction and the finest has 226 cells. The grid used for the computations in this thesis (for $H/D = 2$) is the grid with 146 cells in y. As depicted this grid yields almost identical results to the highly resolved grid, with respect to both first and second order statistics (less than 5% deviation). The near-wall node is for this grid located $0.0009D$ from the wall. The average grid spacing in the y-direction is, as a comparison, $0.0138D$. (For more details on the influence from discretization see Hällqvist & Fuchs 2005*a*,*b*)

6.3. Sampling errors

The convergence of statistical moments depends on the number of statistically independent samples. Higher order moments demand greater number of samples, i.e. longer computational time, as compared to lower order moments. When evaluating LES results it is important to be familiar with the size of the sampling errors associated to the statistical moments, since this group of errors may render the computational results meaningless. The sampling error ε for the mean X of a stochastic variable x can, according to Johansson & Alfredsson (1988), be expressed as

$$\varepsilon(X) = \frac{1}{\sqrt{N}} \frac{x_{rms}}{X_m}, \tag{6.16}$$

where N is the total number of statistically independent samples and X_m the converged mean value ($X_m = \lim \frac{1}{N} \sum_{n=1}^{N} x_n$, $N \to \infty$).

The error due to the finite computational time is within this work chosen to be of similar magnitude as the numerical error (derived from grid refinement), i.e. of the order of $2 - 4\%$.

CHAPTER 7

Results

In this chapter the primal results obtained within this work are briefly presented. A more thorough discussion of the results are given in the enclosed papers in part two of this thesis.

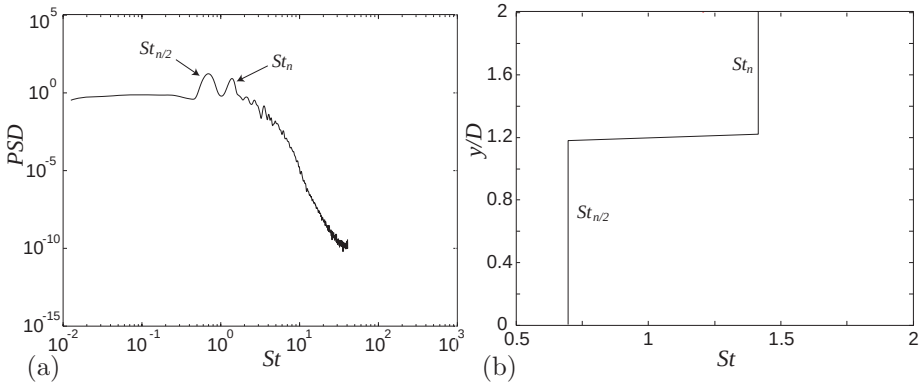

FIGURE 7.1. Power Spectral Density (PSD) for u' in the jet shear-layer at $y/D = 1$ in (a) and evolution of the dominant frequencies within the shear-layer in (b).

7.1. Flow field characteristics of the impinging jet

With a nozzle-to-plate spacing (H/D) of two the proximal region of the impinging jet is characterized by a free jet. Thus, the flow can evolve without influence from the impingement wall to approximately $1D$ downstream of the nozzle. During this evolvement the initial randomly perturbed velocity field develops coherent structures that represent the energetic scales of the flow. Additional to these large scale structures there are a wide range of irregular, less energetic, scales. The spectrum in figure 7.1(a) depicts the distribution of energy among the different temporal scales within the annular shear-layer $1D$ above the wall. The left peak is associated to the subharmonic mode ($St_{n/2}$) of the jet and the right peak is associated to the natural mode of the jet (St_n),

where St is the Strouhal number, based on the diameter of the nozzle and the mean velocity at the nozzle. The former mode represents the primary vortices and the latter the shear-layer mode of the axial jet. In figure 7.1(b) the evolution of dominant modes within the annular shear-layer is depicted. Close to the nozzle the shear-layer mode is dominating. Farther downstream at approximately $y/D = 1.2$ the energy of the subharmonic mode becomes similar to the natural mode. At this location the vortex pairing process take place. From this location and downstream the subharmonic is the dominant frequency. If the nozzle-to-plate spacing would have been larger a second pairing event would take place, whereas, the fundamental mode of the axial jet (i.e. the jet column mode) would become dominant. For the present spacing this pairing event occurs within the wall jet. These results clearly indicate that the natural mode as well as the fundamental mode of the free jet can be captured and accurately predicted.

The primary vortices are convected downstream, along the wall, and may initiate counter rotating secondary vortices. These secondary vortices may, in turn, induce local flow separation which, as will be seen in the coming section, has strong influence on the wall heat transfer.

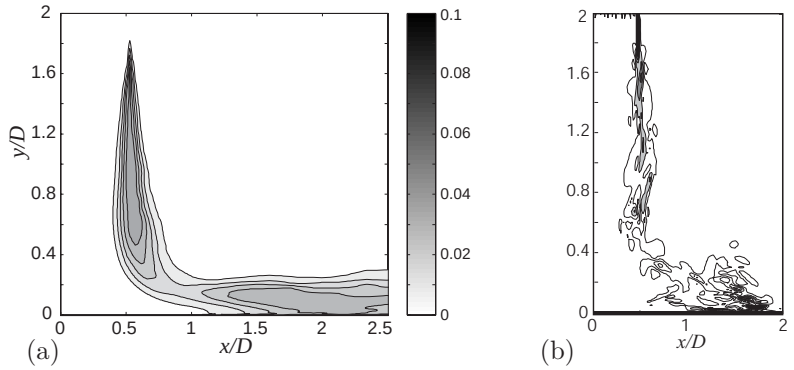

FIGURE 7.2. Turbulent kinetic energy k in the xy-plane in (a) and instantaneous vorticity in the xy-plane in (b).

On an average perspective the flow features, as depicted in figure 7.2(a), negligible levels of turbulent kinetic energy, k, close to the nozzle. This is partly attributed to the inflow conditions, which here are represented by the randomly perturbed top-hat profile. The shear-layer close to the nozzle is, as depicted in figure 7.2(b), of a steady character. At approximately $y/D = 1.8$ the shear-layer becomes highly unsteady and, consequently, the level of k becomes high. The shear-layer grows in size when going downstream. As the wall starts to influence the flow the growth of structures weakens. This can be seen from

the locally low level of k in the region where the shear-layer is deflected by the wall. In the wall jet the strong influence from shear contributes to high production of k. Maximum level of k is obtained in the region around $x/D = 2$. From the vorticity plot one can identify intense vortical motion within the corresponding region. The high level of vorticity originates from primary and secondary vortices.

As seen from the above results the flow character of the impinging jet is inherently unsteady and features formation of coherent structures. It has also been shown that the annular shear-layer features coalescence of vortices. The resulting larger vortex is long-lived and influences the flow character in the wall jet by initiating formation of secondary vortices. Further details on the basic character of the impinging jet are found in **Paper 1**.

7.2. Heat transfer characteristics of the impinging jet

The heat transfer of the impinging jet is influenced by convection by the unsteady flow and molecular diffusion. The latter mechanism is important where the mean velocity is low, such as in the near-wall region. The coherent structures, discussed in the former section, are efficient in mixing and transporting heat. However, contrary to turbulent motion, the coherent structures may have a negative effect on the wall heat transfer. This is determined by the sense of rotation of these structures. In the present studies the flow at the nozzle is at high temperature and the wall is cold. Thus, a counter rotating secondary vortex has a positive effect on the wall heat transfer as it entrains hot fluid towards the wall at its leading edge (downstream most side). This is illustrated by the instantaneous velocity fields in figure 7.3. From the instantaneous vorticity in figure 7.3(a) the secondary vortex (SV) rotates clockwise and contribute, thus, to the local maximum in Nu at $x/D = 1.7$. As also can be seen, the secondary vortex results in local flow separation, as the friction coefficient is negative within this region. The counterclockwise rotating primary vortex (PV) is located above and slightly upstream of the secondary vortex. As seen from the behavior of the friction coefficient and the Nusselt number they correlate perfectly upstream of separation. This indicates that the Reynolds analogy (i.e. $Nu \propto C_f$), in this region of the wall jet, is of relevance. Downstream of the reattachment point weaker correlation is observed, owing to higher rate of irregular structures.

The local flow separation and flow character is more clearly illustrated by figure 7.3(b). From these figures one may conclude that for this specific nozzle-to-plate spacing of two the wall heat transfer is, for small radius, essentially influenced by mean flow convection and the coherent structures. The secondary vortices have a positive effect on the wall heat transfer. The influence from turbulence increases successively with increasing radius. However, due to the local lack of adequate spatial resolution (in the far-field) in addition to the

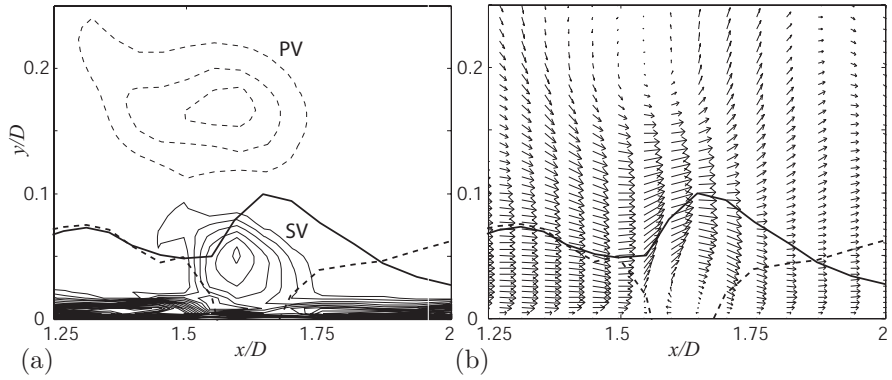

FIGURE 7.3. Enlarged views of the separation region at an arbitrary instant of time. The instantaneous vorticity is depicted in (a) and velocity vectors are depicted in (b). (—): normalized Nusselt number, (- - -): normalized friction coefficient.

influence from the outflow boundary, the far-field character of the wall jet has not been studied.

By increasing the nozzle-to-plate spacing the character of the wall heat transfer changes. For $H/D = 2$ the core region of the axial jet is not influenced by the annular shear-layer. Hence, the character of the flow in the stagnation region is similar to that within the potential core. This results, most frequently, in a Nusselt number distribution featuring a minimum at the stagnation point. For somewhat larger radius a local maximum is obtained. The minimum is attributed to low level of fluctuations and the maximum is, on an average perspective, attributed to a local thinning of the thermal boundary layer (associated to the strongly accelerating wall jet). From a dynamical perspective this maximum is also influenced by the primary vortices formed within the annular shear-layer. These structures penetrate the laminar-like wall jet and augment the near-wall shear, and thus also the Nusselt number. For larger H/D, for which the potential core does not impinge onto the wall, the flow in the stagnation region features high levels of fluctuations. This results in maximum in heat transfer at the stagnation point. For increasing radius the Nusselt number decreases, more or less, monotonically. The precise character of the stagnation heat transfer depends also strongly on the inflow conditions. For more details on heat transfer mechanisms and heat transfer characteristics see **Paper 2**.

7.3. The effect from inflow conditions

As already discussed the inflow conditions have strong influence on the dynamical character of the flow and, hence, also on the wall heat transfer. This is

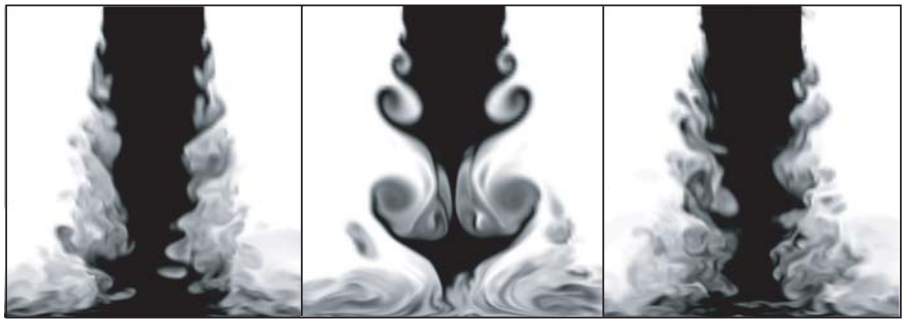

FIGURE 7.4. Influence from boundary conditions on the instantaneous scalar field for $H/D = 4$. The left, middle and right picture shows the resulting flow field from a top-hat profile with imposed random perturbations, a mollified profile with imposed random perturbations and fully developed turbulent inflow condition, respectively.

particularly so for small H/D, as the axial jet is not allowed to develop. For sufficiently large H/D (larger than the potential core) the flow that impinges onto the wall is, more or less, unaffected by the inflow conditions.

To illustrate the overall influence from inflow conditions instantaneous visualizations of the scalar concentration, for impinging jets with a nozzle-to-plate spacing of four jet diameters, are depicted in figure 7.4. In this figure effects from, both, the mean velocity profile and the perturbations are considered. The left most picture shows the flow field resulting from a randomly perturbed top-hat profile. The middle picture shows the corresponding results for a randomly perturbed mollified profile and the right picture shows the corresponding results for fully developed turbulent inflow condition. As can be seen the applied top-hat profile produces much higher correlation to the fully turbulent case than the mollified profile. The weakly mollified profile yields, to a greater extent, formation of large scale axisymmetric vortices, whereas the two other cases behave in a more diffusive manner with a large amount of small irregular structures, i.e. more turbulent like. As a conclusion from this illustration, the randomly perturbed top-hat profile is a very good candidate in emulating turbulent inflow conditions.

A more detailed assessment of the influence from the inflow conditions are depicted in figure 7.5. This figure clearly indicates the importance of appropriate inflow conditions. As seen, with fully developed turbulent inflow condition the agreement with the experimental results by Cooper *et al.* (1993) at $x/D = 1$ in figure 7.5(a) is very good. In this experiment the flow at the nozzle was generated by fully developed pipe flow ($80D$ long). The randomly

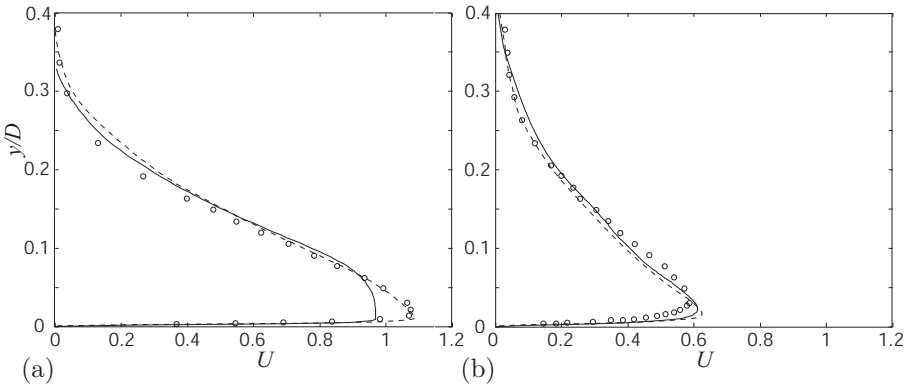

FIGURE 7.5. Mean radial velocity at $x/D = 1$ in (a) and at $x/D = 2.5$ in (b) ($Re = 20000$, $H/D = 2$). (—): Random perturbed top-hat profile, (- - -): fully developed turbulent inflow condition, (∘): experimental data by Cooper *et al.* (1993) ($Re = 23000$, fully developed pipe flow).

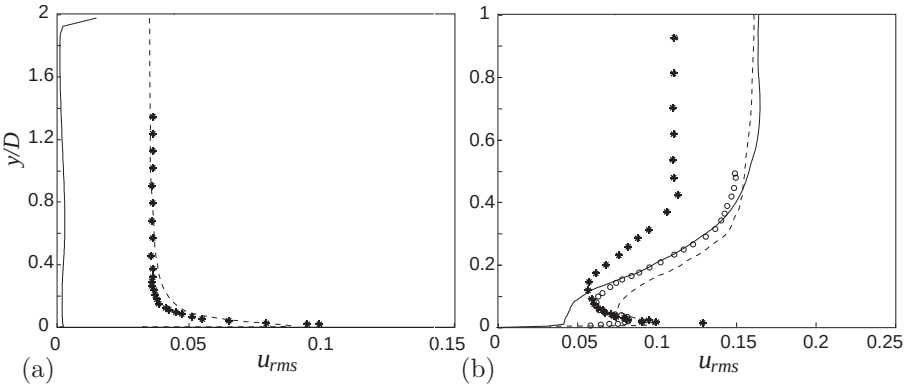

FIGURE 7.6. Radial perturbation velocity (u_{rms}) at $x/D = 0$ in (a) and at $x/D = 0.5$ in (b) ($Re = 20000$, $H/D = 2$). (—): Random perturbed top-hat profile, (- - -): fully developed turbulent inflow condition, (∘): experimental data by Cooper *et al.* (1993), (∗): experimental data by Geers *et al.* (2004) ($Re = 23000$, fully developed pipe flow).

perturbed top-hat profile yields a velocity profile with lower velocity in the near-wall region. Further downstream at $x/D = 2.5$ in figure 7.5(b) the two

simulations yield almost identical results. This is due to the natural development of the flow. The agreement with the experimental results at this station is somewhat less good.

The influence on turbulent statistics is more pronounced than on the mean flow. This becomes particularly clear when studying the flow character at small distances from the jet axis. Figure 7.6 depicts the radial perturbation velocity along the stagnation line and in the annular shear-layer. Along the stagnation line in figure 7.6(a) the top-hat case features negligible level of fluctuations. With turbulent inflow conditions though, the level of u_{rms} is almost identical to that measured by Geers *et al.* (2004). The higher level of turbulence within the stagnation region with turbulent inflow conditions has naturally a positive effect on the wall heat transfer. In the shear-layer in figure 7.6(b) the discrepancy between the two computations are not as pronounced. Only in the near-wall region the top-hat case fails in predicting the correct behavior. The turbulent case and the experiments exhibit a local peak of u_{rms} near the wall. The agreement with the data by Cooper *et al.* (1993) is, at this station, overall higher relative to the data by Geers *et al.* (2004).

The present results indicate that the inflow conditions are of significant importance. To obtain data that features high correlation with experimental data on turbulent impinging jets, turbulent inflow conditions are needed. This is particularly so for turbulent quantities in the center most regions. The results also indicate that two, practically, identical experiments may provide results that do not fully agree. This might be associated to different experimental setups (i.e. jet nozzle conditions) and the different measurement techniques. For further details on the influence from inflow boundary conditions see **Paper 5** and **Paper 6**.

7.4. Effects of swirl

When swirl is applied to the nozzle outlet an additional mean velocity component becomes important, i.e. the azimuthal velocity component. This results in additional shear forces, why the resulting force vector will be directed with an angle, with respect to the inlet plane, determined by the swirl number, S. The swirl number is here defined as the ratio between the azimuthal velocity at $r = D/2$ and the mean axial velocity, V_0. Three different swirl numbers have been considered, i.e. $S = 0$, $S = 0.5$ and $S = 1$. The azimuthal velocity is here applied as solid body rotation. The axial velocity is given by the randomly perturbed top-hat profile (cf. **Paper 3**).

The results for $S = 0$ and $S = 0.5$ do not differ much. However, with high swirl, i.e. $S = 1$, the spreading of the jet becomes as strong as a recirculation bubble is formed. This bubble results, as depicted in figure 7.7, in reversed flow along the stagnation line for $y/D < 0.6$. The flow character within this bubble is highly unsteady. Despite the high level of fluctuations, the wall heat transfer in the stagnation region is as, depicted in figure 7.8, low. The low

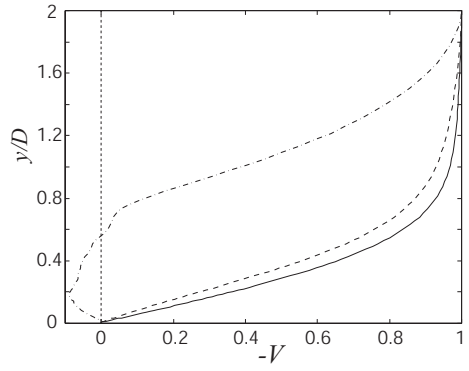

FIGURE 7.7. Mean axial velocity decay along the stagnation line (Re=20000, $H/D = 2$). (—): $S = 0$, (- - -): $S = 0.5$, (- · -): $S = 1$.

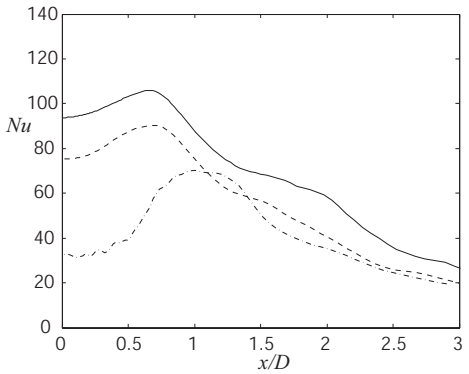

FIGURE 7.8. Local Nusselt number as function of x/D (Re=20000, $H/D = 2$). (—): $S = 0$, (- - -): $S = 0.5$, (- · -): $S = 1$.

levels of Nu are attributed to the insignificant contribution from mean flow convection. Thus, in order to obtain high rates of wall heat transfer in the stagnation region of swirling impinging jets the spreading of the flow must be controlled. A negative influence from swirl on wall heat transfer was also found by Lee *et al.* (2002*b*).

However, swirl may also have a positive effect on the wall heat transfer. This has been concluded by e.g. Wen & Jang (2003). The influence on the flow in the stagnation region is not completely given by the swirl number itself. The radial distribution of the mean velocity components and the character of

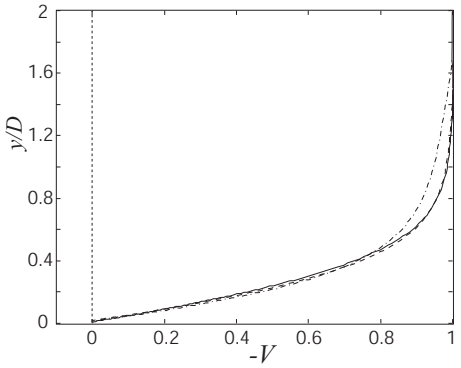

FIGURE 7.9. Mean axial velocity decay along the stagnation line for turbulent inflow conditions (Re=20000, $H/D = 2$). (—): $S = 0$, (- - -): $S = 0.5$, (- · -): $S = 1$.

the inflow perturbations are all essential. In **Paper 6** the boundary conditions have been determined from separate simulations of rotating turbulent pipe flow. When comparing the results from these simulations with other inlet conditions (i.e. those originating from solid body rotation) some major differences are observed. Even for a high level of swirl the spreading of the axial jet with fully developed turbulent inflow condition is, as depicted in figure 7.9, low. This in combination with the high level of fluctuations results in high levels of heat transfer within the stagnation region. As depicted in figure 7.10 the maximum stagnation Nusselt number is attained for the highly swirling case. For larger radii the influence from swirl diminish. The non-swirling case yields, for $x/D > 1$, overall slightly higher level of wall heat transfer. This is attributed to the weaker spreading of the axial jet, since a higher spreading rate results in a wider wall jet. A wider wall jet features a weaker near-wall sher-layer, and consequently also a more gradual thermal boundary layer.

We have also considered the influence of swirl on annular impinging jets (cf. **Paper 4**). This setup is, with respect to the character of the mean velocity profiles and superimposed perturbations, similar to that in **Paper 3**. The results from this study show similar trends to those discussed above, i.e. with high level of swirl the Nusselt number for small radius (approximately smaller than $x/D = 1.4$) becomes obstructed. For larger radii the influence from the applied swirl is weak. Relative to the circular swirling jet (solid body rotation), the annular configuration yields slightly higher rate of heat transfer in the stagnation region for the non-swirling and the strongly swirling cases. This is attributed to the rate of fluctuations and the character of the mean flow. The level and character of the imposed swirl is not only essential for the rate of wall heat transfer. The dynamical behavior of the flow is also significantly affected.

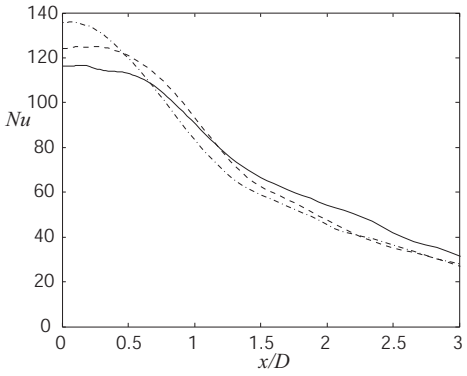

FIGURE 7.10. Local Nusselt number as function of x/D for turbulent inflow conditions (Re=20000, $H/D = 2$). (—): $S = 0$, (- - -): $S = 0.5$, (- · -): $S = 1$.

The formation of coherent structures has shown to become less distinct with increasing level of swirl.

CHAPTER 8

Industrial significance

This work represents a pre-development project initiated by Scania CV AB and KTH (Royal Institute of Technology). The main objectives of this project are to increase the competence on numerical simulations of unsteady flows with emphasis on large eddy simulation, turbulence and heat transfer mechanisms. This thesis provides, from both an academic and an industrial point of view, insight into all these areas of interest. The results summarized in this thesis are directly beneficial for several components in trucks, such as engine cooling, cooling of electronics and heating/cooling of materials.

The impinging jet is represented in a great number of applications. The most evident one, closely related to this work, is the cooling air flow that impinges onto the engine. The geometry of the engine is however, in relation to the studied geometry, far more complex. More relevant is the cooling of the heat exchangers installed in front of the fan and the engine. Cooling of a heat exchanger, for instance a radiator, involves both impinging and wall parallel flows. Thus, the same mechanisms discussed in this thesis are present also for this application. Besides from cooling and heating the impinging jet is also represented by the fuel injected into the engines combustion chamber.

A truck, and of course several other engineering applications, involve a great number of parts for which sufficient cooling is a necessity. As the considered range of impinging jets covers different types of flows and involve different heat transfer mechanisms the knowledge and understanding gained from this study can directly be transferred to the more complex industrial applications.

CHAPTER 9

Conclusions

This thesis covers some of the basic characteristics in numerical simulation of impinging jets with heat transfer. The performed simulations feature, to begin with, the simplest kind of inflow conditions, i.e. a randomly perturbed top-hat velocity profile. The flow and scalar fields of this simulation have been studied in some detail and are summarized in **Paper 1** and **Paper 2** in this thesis. In the thereafter following work the influence from swirl (solid body rotation) was studied for both circular (cf. **Paper 3**) and annular impinging jets (cf. **Paper 4**). The next step was to enhance the study by introducing explicit forcing of discrete frequency components. The character of the applied forcing was decided on the basis of the natural frequency of the jet. Both the natural mode plus harmonics and off-harmonics of this mode were excited. Additional to the periodically forced top-hat profile also a periodically forced smoothed profile was studied. Flow field statistics and heat transfer characteristics for these cases are summarized in **Paper 5** in this thesis. In the final and most sophisticated study the demands on computer hardware was increased as it involved precursor simulations of turbulent pipe flow. These precursor simulations were carried out in order to construct turbulent inflow conditions for the impinging jet simulations. The results on turbulent jet impingement are summarized in **Paper 6** in this thesis. In this paper also the influence from nozzle-to-plate spacing, Reynolds number and swirl are discussed.

The results presented in this thesis represent a broad coverage of impinging jets for a variety of different flow configurations. Detailed descriptions, both quantitatively and qualitatively, on the basic heat transfer mechanisms have been given. The influence from the geometrical parameter H/D has been isolated. The nozzle-to-plate spacing has strong influence on the flow character, both within the axial jet and within the wall jet. Small spacing results in an abrupt deflection of the axial jet and, thus, the wall boundary layer becomes thin and the wall heat transfer becomes high. For large spacing the axial jet develops without influence from the wall, why the impinging flow will be less influenced by the inflow conditions and also of a more turbulent character.

The influence from swirl on wall heat transfer depends strongly on the applied conditions. The production of turbulence increases with swirl, which is positive for the wall heat transfer. However, with increased level of swirl also

the spreading of the jet increases, which have a negative effect on the wall heat transfer. For the simplest case, featuring solid body rotation, the stagnation point heat transfer decreases with swirl, whereas for the inlet conditions originating from the rotating pipe simulation, the stagnation point heat transfer increases.

It has been shown that the character of the inflow boundary conditions has a dramatic influence on the dynamical and statistical character of the flow field. A small change of the mean velocity profile may result in a flow field of completely different character. This is particularly important if the region of interest is in the close vicinity of the inflow. Turbulent inflow conditions have shown to be of significant importance for small radius, particularly in case of swirling impinging jets. For non-swirling flows and outside of the core region of the axial jet the more simple randomly perturbed top-hat condition yields results comparable to the turbulent counterpart. From the comparisons with experimental data it is evident that implicit large eddy simulation can be used to accurately predict turbulent flows, provided that the flow is adequately resolved.

Possible extensions to this introductory work should involve further modeling aspects, as well as means for controlling and optimizing the heat transfer properties of impinging jets. Furthermore, some additional studies on swirling impinging jets are needed in order to more precisely asses the influence from the inflow conditions, i.e. with respect to the radial distribution of the mean velocity components and the character of the fluctuating field. This study is essential as many industrial cooling/heating applications feature swirling jet impingement.

CHAPTER 10

Papers and authors contributions

Paper 1

Numerical study of impinging jets. Flow field characteristics
T. Hällqvist (TH) & L. Fuchs (LF).

This paper summarizes the results for a circular impinging air jet at $Re_D = 20000$ featuring a randomly perturbed top-hat inflow profile and a nozzle-to-plate spacing of two jet diameters. The objectives are to describe the average properties of the flow and also some dynamical features. The LES code was provided by LF and the paper was written by TH under supervision by LF.

Paper 2

Numerical study of impinging jets. Heat transfer characteristics
T. Hällqvist & L. Fuchs.

This paper is a continuation of **Paper 1** and describes the dynamical character and heat transfer mechanisms of the impinging air jet.

Paper 3

Numerical study of swirling impinging jets with heat transfer
T. Hällqvist & L. Fuchs.

This paper deals with swirling circular impinging jets. The velocity inlet is applied with solid body rotation. The influence from the level of swirl on the flow and scalar fields are studied. This paper was written by TH under supervision by LF. The numerical code is the same as in the former papers. This paper was presented by TH at ASME Heat Transfer/Fluids Engineering Summer Conference in Charlotte, USA, July 2004.

Paper 4

Numerical study of swirling and non-swirling annular impinging jets with heat transfer
T. Hällqvist & L. Fuchs.

The results presented in this paper is a continuation of **Paper 3** and deals with swirling annular impinging jets. This paper was written by TH under supervision by LF. The numerical code is the same as in the former papers. This

paper was presented by TH at the 17th AIAA Computational Fluid Dynamics Conference in Toronto, Canada, June 2005.

Paper 5

Characteristics of forced circular impinging jets
T. Hällqvist & L. Fuchs.

In this paper the randomly perturbed inflow conditions are complemented by periodic forcing. Two mean velocity profiles are considered, the top-hat and the smooth profiles. The nozzle-to-plate spacing is two and the Reynolds number is 20000. In this paper the dynamical character of the flow as well as the wall heat transfer are studied. This paper was written by TH under supervision by LF. The numerical code is the same as in the former papers.

Paper 6

Large eddy simulation of impinging jets with emphasis on the inflow conditions
T. Hällqvist & L. Fuchs.

In this paper the main focus is on the inflow conditions. Additional to the simple, former considered approaches, also turbulent inflow conditions are applied. The influence from nozzle-to-plate spacing, Reynolds number, mollification and swirl are also studied. Both flow and heat transfer characteristics are discussed. This paper was written by TH under supervision by LF. The numerical code is the same as in the former papers.

Acknowledgements

I would like to thank my supervisor, Prof. Laszlo Fuchs, for his help and support throughout this work.

I wish to thank all my colleagues at KTH and at Scania for their support and friendship. Special thanks are dedicated to my room mate Ola Lögdberg and my reference group at Scania, composed by Dr. Lars Dahlén, Dr. Per Elofsson, Dr. Per-Arne Eriksson, Claes Erixon, Per Jonsson and Hasse Wikström.

I would also like to thank Stephen Conway (Scania CV AB) and Christian Svensson (CARAN) for commenting the manuscript.

The personnel at the library at Scania are acknowledged for helping me with articles, books etc.

I wish to thank my family and all my friends for their support and understanding.

Last, but not least, I would like to thank my employer Scania CV AB for making my doctoral studies possible.

References

Anderson, S. L. & Longmire, E. K. 1995 Particle motion in the stagnation zone of an impinging jet. *J. Fluid Mech.* **299**, 333–366.

Angioletti, M., Di Tommaso, R. M., Nino, E. & Ruocco, G. 2003 Simultaneous visualization of flow field and evaluation of local heat transfer by transitional impinging jets. *Int. J. Heat Mass Transf.* **46**, 1703–1713.

Arganbright, D. G. & Resch, H. 1971 A review of basic aspects of heat transfer under impinging air jets. *Wood Sci. Tech.* **5**, 73–94.

Ashforth-Frost, S., Jambunathan, K. & Whitney, C. F. 1997 Velocity and turbulence characteristics of a semiconfined orthogonally impinging slot jet. *Exp. Thermal Fluid Sci.* **14**, 60–67.

Bardina, J., Ferziger, J. H. & Reynolds, W. C. 1980 Improved subgrid scale models for large eddy simulation. *AIAA Paper 80-1357*.

Bardina, J., Ferziger, J. H. & Reynolds, W. C. 1983 Improved turbulence models based on large eddy simulation of homogeneous, incompressible, turbulent flows. Report TF-19, Thermosciences Division, Dept. Mechanical Engineering, Stanford University.

Batchelor, G. K. & Gill, A. E. 1962 Analysis of the stability of axisymmetric jets. *J. Fluid Mech.* **14**, 529–551.

Baughn, J. W. & Shimizu, S. 1989 Heat transfer measurements from a surface with uniform heat flux and an impinging jet. *ASME J. Heat Transf.* **111**, 1096–1098.

Baukal, C. E. & Gebhart, B. 1997 Surface condition effects on flame impingement heat transfer. *Exp. Thermal Fluid Sci.* **15**, 323–335.

Behnia, M., Parneix, S., Shabany, Y. & Durbin, P. A. 1999 Numerical study of turbulent heat transfer in confined and unconfined impinging jets. *Int. J. Heat Fluid Flow* **20**, 1–9.

Beitelmal, A. H., Saad, M. A. & Patel, C. D. 2000 Effects of surface roughness on the average heat transfer of an impinging air jet. *Int. Comm. Heat Mass Transf.* **27**, 1–12.

Billant, P., Chomaz, J.-M. & Huerre, P. 1998 Experimental study of vortex breakdown in swirling jets. *J. Fluid Mech.* **376**, 183–219.

Brancher, P., Chomaz, J. M. & Huerre, P. 1994 Direct numerical simulations of round jets: Vortex induction and side jets. *Phys. Fluids* **6**, 1768–1774.

Brandt, T. 2004 Studies on numerical errors in large eddy simulation. Licentiate thesis, Report A-22, Helsinki University of Technology. Laboratory of Aerodynamics.

Brignoni, L. A. & Garimella, S. V. 2000 Effects of nozzle-inlet chamfering on pressure drop and heat transfer in confined air jet impingement. *Int. J. Heat Mass Transf.* **43**, 1133–1139.

Chan, T. L., Leung, C. W., Jambunathan, K., Ashforth-Frost, S., Zhou, Y. & Liu, M. H. 2002 Heat transfer characteristics of a slot jet impinging on a semi-circular convex surface. *Int. J. Heat Mass Transf.* **45**, 993–1006.

Chow, F. K., & Moin, P. 2003 A further study of numerical errors in large-eddy simulations. *J. Comp. Phys.* **184**, 366–380.

Chun, D. H. & Schwarz, W. H. 1967 Stability of the plane incompressible viscous wall jet subjected to small disturbances. *Phys. Fluids* **10**, 911–915.

Cohen, J., Amitay, M. & Bayly, B. J. 1992 Laminar-turbulent transition of wall-jet flows subjected to blowing and suction. *Phys. Fluids A* **4**, 283–289.

Cohen, J. & Wygnanski, I. 1987 The evolution of instabilities in the axisymmetric jet. Part 1. The linear growth of disturbances near the nozzle. *J. Fluid Mech.* **176**, 191–219.

Colucci, D. W. & Viskanta, R. 1996 Effects of nozzle geometry on local convective heat transfer to a confined impinging air jet. *Exp. Thermal Fluid Sci.* **13**, 71–80.

Cooper, D., Jackson, D. C., Launder, B. E. & Liao, G. X. 1993 Impinging jet studies for turbulence model assessment-I. Flow-field experiments. *Int. J. Heat Mass Transf.* **36**, 2675–2684.

Cornaro, C., Fleischer, A. S. & Goldstein, R. J. 1999 Flow visualization of a round jet impinging on cylindrical surfaces. *Exp. Thermal Fluid Sci.* **20**, 66–78.

Craft, T. J., Graham, L. J. W. & Launder, B. E. 1993 Impinging jet studies for turbulence model assessment-II. An examination of the performance of four turbulence models. *Int. J. Heat Mass Transf.* **36**, 2685–2697.

Crow, S. C. & Champagne, F. H. 1971 Orderly structure in jet turbulence. *J. Fluid Mech.* **48**, 547–591.

da Silva, C. B. & Pereira, C. F. 2004 The effect of subgrid-scale models on the vortices computed from large-eddy simulation. *Phys. Fluids* **16**, 4506–4534.

Danaila, I. & Boersma, B. J. 2000 Direct numerical simulation of bifurcating jets. *Phys. Fluids* **12**, 1255–1257.

Danaila, I., Dušek, J. & Anselmet, F. 1997 Coherent structures in a round, spatially evolving, unforced, homogeneous jet at low Reynolds numbers. *Phys. Fluids* **9**, 3323–3342.

Davidson, L. & Peng, S. H. 2003 Hybrid LES-RANS modelling: a one-equation SGS model combined with a $k-\omega$ model for predicting recirculating flows. *Int. J. Num. Meth. Fluids* **43**, 1003–1018.

Dejoan, A. & Leschziner, M. A. 2005 Large eddy simulation of a plane turbulent wall jet. *Phys. Fluids* **17**, 025102–1–025102–16.

Dianat, M., Fairweather, M. & Jones, W. P. 1996 Predictions of axisymmetric and two-dimensional impinging turbulent jets. *Int. J. Heat Fluid Flow* **17**, 530–538.

Didden, N. & Ho, C.-M. 1985 Unsteady separation in a boundary layer produced by an impinging jet. *J. Fluid Mech.* **160**, 235–256.

Drubka, R. E., Reisenthel, P. & Nagib, H. M. 1989 The dynamics of low initial disturbance turbulent jets. *Phys. Fluids A* **1**, 1723–1735.

Facciolo, L. 2003 Experimental study of rotating pipe and jet flows. Licentiate thesis 2003:15, Dept. Mechanics, Royal Institute of Technology, Stockholm.

Ferziger, J. H. & Peric, M. 2001 *Computational methods for fluid dynamics.* Springer-Verlag.

Fletcher, C. A. J. 1988 *Computational techniques for fluid dynamics 2.* Springer-Verlag.

Fondse, H., Leijdens, H. & Ooms, G. 1983 On the influence of the exit conditions on the entrainment rate in the development region of a free, round, turbulent jet. *Appl. Sci. Research* **40**, 355–375.

Friedrich, R., Hüttl, T. J., Manhart, M. & Wagner, C. 2001 Direct numerical simulation of incompressible turbulent flows. *Comput. & Fluids* **30**, 555–579.

Fureby, C. & Grinstein, F. F. 2002 Large eddy simulation of high-Reynolds-number free and wall-bounded flows. *J. Comp. Phys.* **181**, 68–97.

Garimella, S. V. & Nenaydykh, B. 1996 Nozzle-geometry effects in liquid jet impingement heat transfer. *Int. J. Heat Mass Transf.* **39**, 2915–2923.

Geers, L. F. G., Tummers, M. J. & Hanjalic, K. 2004 Experimental investigation of impinging jet arrays. *Exp. Fluids* **36**, 946–958.

Germano, M., Piomelli, U., Moin, P. & Cabot, W. H. 1991 A dynamic subgrid-scale eddy viscosity model. *Phys. Fluids A* **3**, 1760–1765.

Geurts, B. J. 2003 *Elements of direct and large-eddy simulation*. R.T. Edwards, Inc.

Ginevsky, A. S., Vlasov, Ye. V. & Karavosov, R. K. 2004 *Acoustic control of turbulent jets*. Springer-Verlag.

Gullbrand, J. 2002 Grid-independent large-eddy simulation in turbulent channel flow using three-dimensional explicit filtering. *Annual Research Briefs,* pp. 167–179. Center for Turbulence Research, NASA Ames-Stanford University.

Gullbrand, J. & Chow, F. K. 2002 Investigation of numerical errors, subfilter-scale models, and subgrid-scale models in turbulent channel flow simulations. Proceedings of the Summer Program, pp. 87–104. Center for Turbulence Research, NASA Ames-Stanford University.

Gullbrand, J. & Chow, F. K. 2003 The effect of numerical errors and turbulence models in large-eddy simulations of channel flow, with and without explicit filtering. *J. Fluid Mech.* **495**, 323-341.

Hall, J. W. & Ewing, D. 2005 The development of the large-scale structures in round impinging jets exiting long pipes at two Reynolds numbers. *Exp. Fluids* **38**, 50–58.

Harvey, J. K. & Perry, F. J. 1971 Flow field produced by trailing vortices in the vicinity of the ground. *AIAA J.* **9**, 1659–1660.

Held, J. & Fuchs, L. 1997 Large eddy simulation of compressible separated flow around a NACA 0012 wing section. *AIAA Paper 97-1931.*

Ho, C. M. & Huang, L. S. 1982 Subharmonics and vortex merging in mixing layers. *J. Fluid Mech.* **119**, 443–479.

Ho, C.-M. & Nossier, N. 1981 Dynamics of an impinging jet. Part 1. The feedback phenomenon. *J. Fluid Mech.* **105**, 119–142.

Hourigan, K., Rudman, M. & Brocher, E. 1996 The feedback loop in impinging and two-dimensional high-subsonic and supersonic jets. *Exp. Thermal Fluid Sci.* **12**, 265–270.

Hsiao, F.-B., Chou, Y.-W. & Huang, J.-M. 1999 The study of self-sustained oscillating plane jet flow impinging upon a small cylinder. *Exp. Fluids* **27**, 392–399.

Hsiao, F.-B., Hsu, I.-C. & Huang, J.-M. 2004 Evolution of coherent structures and feedback mechanism of the plane jet impinging on a small cylinder. *J. Sound Vibr.* **278**, 1163–1179.

Huang, L. & El-Genk, M. S. 1998 Heat transfer and flow visualization experiments of swirling, multi-channel, and conventional impinging jets. *Int. J. Heat Mass Transf.* **41**, 583–600.

Hussain, A. K. M. F. 1983 Coherent structures - reality and myth. *Phys. Fluids* **26**, 2816–2850.

Hussein, H. J., Capp, S. & George, W. K. 1994 Velocity measurements in a high-Reynolds-number, momentum-conserving, axisymmetric, turbulent jet. *J. Fluid Mech.* **258**, 31–75.

Hwang, S. D. & Cho, H. H. 2003 Effects of acoustic excitation positions on heat transfer and flow in axisymmetric impinging jet: main jet excitation and shear layer excitation. *Int. J. Heat Fluid Flow* **24**, 199–209.

Hwang, S. D., Lee, C. H. & Cho, H. H. 2001 Heat transfer and flow structures in axisymmetric impinging jet controlled by vortex pairing. *Int. J. Heat Fluid Flow* **22**, 293–300.

Hällqvist, T. & Fuchs, L. 2004 Numerical study of swirling impinging jets with heat transfer. *ASME HTFED 04-56478.* **Paper 3**.

Hällqvist, T. & Fuchs, L. 2005*a* Numerical study of impinging jets. Flow field characteristics. **Paper 1**.

Hällqvist, T. & Fuchs, L. 2005*b* Numerical study of impinging jets. Heat transfer characteristics. **Paper 2**.

Hällqvist, T. & Fuchs, L. 2005*c* Numerical study of swirling and non-swirling annular impinging jets with heat transfer. *AIAA Paper 05-5153*. **Paper 4**.

Hällqvist, T. & Fuchs, L. 2006*a* Characteristics of forced circular impinging jets. **Paper 5**.

Hällqvist, T. & Fuchs, L. 2006*b* Large eddy simulation of impinging jets with emphasis on the inflow conditions. **Paper 6**.

Imao, S., Itoh, M. & Harada, T. 1996 Turbulent characteristics of the flow in an axially rotating pipe. *Int. J. Heat Fluid Flow* **17**, 444–451.

Johansson, A. V. & Alfredsson, P. H. 1988 Experimental methods in fluid mechanics. Dept. Mechanics, Royal Institute of Technology, Stockholm.

Kempf, A., Klein, M. & Janicka, J. 2005 Efficient generation of initial- and inflow-conditions for transient turbulent flows in arbitrary geometries. *Flow Turb. Comb.* **74**, 67–84.

Klein, M., Sadiki, A. & Janicka, J. 2003 A digital filter based generation of

inflow data for spatially developing direct numerical or large eddy simulations. *J. Comp. Phys.* **186**, 652–665.

Knowles, K. & Myszko, M. 1998 Turbulence measurements in radial wall-jets. *Exp. Thermal Fluid Sci.* **17**, 71–78.

Komori, S. & Ueda, H. 1985 Turbulent flow structure in the near field of a swirling round free jet. *Phys. Fluids* **28**, 2075–2082.

Kondo, K., Murakami, S. & Mochida, A. 1997 Generation of velocity fluctuations for inflow boundary condition of les. *J. Wind Eng. Ind. Aero.* **67&68**, 51–64.

Landa, P. S. & McClintock, P. V. E. 2004 Development of turbulence in subsonic submerged jets. *Phys. Rpt.* **397**, 1–62.

Landreth, C. C. & Adrian, R. J. 1990 Impingement of a low Reynolds number turbulent circular jet onto a flat plate at normal incidence. *Exp. Fluids* **9**, 74–84.

Lee, D. H., Lee, Y. M., Kim, Y. T., Won, S. Y. & Chung, Y. S. 2002*a* Heat transfer enhancement by the perforated plate installed between an impinging jet and the target plate. *Int. J. Heat Mass Transf.* **45**, 213–217.

Lee, D. H., Won, S. Y., Kim, Y. T. & Chung, Y. S. 2002*b* Turbulent heat transfer from a flat surface to a swirling round impinging jet. *Int. J. Heat Mass Transf.* **45**, 223–227.

Lee, J. & Lee, S.-J. 2000*a* The effect of nozzle aspect ratio on stagnation region heat transfer characteristics of elliptic impinging jet. *Int. J. Heat Mass Transf.* **43**, 555–575.

Lee, J. & Lee, S.-J. 2000*b* The effect of nozzle configuration on stagnation region heat transfer enhancement of axisymmetric jet impingement. *Int. J. Heat Mass Transf.* **43**, 3497–3509.

Liepmann, D. & Gharib, M. 1992 The role of streamwise vorticicty in the near-field entrainment of round jets. *J. Fluid Mech.* **245**, 643–668.

Liu, T. & Sullivan, J. P. 1996 Heat transfer and flow structures in an excited circular impinging jet. *Int. J. Heat Mass Transf.* **39**, 3695–3706.

Lund, T. S. 2003 The use of explicit filters in large eddy simulation. *Comp. Math. Appl.* **46**, 603–616.

Mankbadi, R. R. 1985 The mechanism of mixing enhancement and suppression in a circular jet under excitation conditions. *Phys. Fluids* **28**, 2062–2074.

Margolin, L.G., Smolarkiewicz, P.K. & Sorbjan, Z. 1999 Large-eddy simulations of convective boundary layers using nonoscillatory differencing. *Phys. D* **133**, 390–397.

Marsden, A. L., Vasilyev, O. V. & Moin, P. 2002 Construction of Commutative Filters for LES on Unstructured Meshes. *J. Comp. Phys.* **175**, 584–603.

Maurel, A., Ern, P., Zielinska, B. J. A. & Wesfreid, J. E. 1996 Experimental study of self-sustained oscillations in a confined jet. *Phys. Rev. E* **54**, 3643–3651.

Meinke, M., Schröder, W, Krause, E. & Rister, Th. 2002 A comparison of second- and sixth-order methods for large-eddy simulations. *Comput. & Fluids* **31**, 695–718.

Meyer, T. R., Dutton, J. C. & Lucht, R. P. 1999 Vortex interaction and mixing in a driven gaseous axisymmetric jet. *Phys. Fluids* **11**, 3401–3415.

Mi, J., Nobes, D. S. & Nathan, G. J. 2001 Influence of jet exit conditions on the passive scalar field of an axisymmetric free jet. *J. Fluid Mech.* **432**, 91–125.

Michalke, A. & Hermann, G. 1982 On the inviscid instability of a circular jet with external flow. *J. Fluid Mech.* **114**, 343–359.

Monkewitz, P. A. & Pfizenmaier, E. 1991 Mixing by "side jets" in strongly forced and self-excited round jets. *Phys. Fluids A* **3**, 1356–1361.

Morris, P. J. 1976 The spatial viscous instability of axisymmetric jets. *J. Fluid Mech.* **77**, 511–529.

Na, Y. & Moin, P. 1998 Direct numerical simulation of a separated turbulent boundary layer. *J. Fluid Mech.* **374**, 379–405.

Olsson, M. 1997 Large eddy simulation of turbulent jets. Doctoral thesis 1999:16, Dept. Mechanics, Royal Institute of Technology, Stockholm.

Olsson, M. & Fuchs, L. 1996 Large eddy simulation of the proximal region of a spatially developing circular jet. *Phys. Fluids* **8**, 2125–2137.

Olsson, M. & Fuchs, L. 1998 Large eddy simulation of a forced semi-confined circular impinging jet. *Phys. Fluids* **10**, 476–486.

Panda, J. & McLaughlin, D. K. 1994 Experiments on the stability of a swirling jet. *Phys. Fluids* **6**, 263–276.

Park, T. S. & Sung, H. J. 2001 Development of a near-wall turbulence model and application to jet impingement heat transfer. *Int. J. Heat Fluid Flow* **22**, 10–18.

Pasquetti, R. 2005 High-order LES modeling of turbulent incompressible flow. *C.R. Mécanique* **333**, 39-49.

Petersen, R. A. 1978 Influence of wave dispersion on vortex pairing in a jet. *J. Fluid Mech.* **89**, 469–495.

Phares, D. J., Smedley, G. T. & Flagan, R. C. 2000 The wall shear stress produced by the normal impingement of a jet on a flat surface. *J. Fluid Mech.* **418**, 351–375.

Pope, S. 2000 *Turbulent flows*. Cambridge university press.

Popiel, C. O. & Trass, O. 1991 Visualization of a free and impinging round jet. *Exp. Thermal Fluid Sci.* **4**, 253–264.

Rai, M. M. & Moin, P. 1991 Direct simulations of turbulent flow using finite-difference schemes. *J. Comp. Phys.* **96**, 15–53.

Raman, G., Zaman, K. B. M. Q. & Rice, E. J. 1989 Initial turbulence effect on jet evolution with and without tonal excitation. *Phys. Fluids A* **1**, 1240–1248.

Revstedt, J. 1999 On the modelling of turbulent flow and mixing in stirred reactors. Doctoral Thesis, Division of Heat Transfer, Department of Heat and Power Engineering, Lund Institute of Technology, Lund.

Rockwell, D. & Naudascher, E. 1979 Self-sustained oscillations of impinging free shear layers. *Ann. Rev. Fluid. Mech.* **11**, 67–94.

Sagaut, P. 2001 *Large eddy simulation for incompressible flows*. Springer-Verlag.

Sarghini, F., Piomelli, U. & Balaras, E. 1999 Scale-similar models for large-eddy simulations. *Phys. Fluids* **11**, 1596–1607.

Sarpkaya, T. 1971 On stationary and travelling vortex breakdown. *J. Fluid Mech.* **45**, 545–559.

Shadlesky, P. S. 1983 Stagnation point heat transfer for jet impingement to a plane surface. *AIAA J.* **21**, 1214–1215.

Smagorinsky, J. 1963 General circulation experiments with the primitive equations. I: The basic experiment. *Month. Weath. Rev.* **91**, 99–165.

Spalart, P. R. 2000 Strategies for turbulence modelling and simulations. *Int. J. Heat Fluid Flow* **21**, 252–263.

Spalart, P. R., Jou, W.-H., Strelets, M. & Allmaras, S.R. 1997 Comments on the feasibility of LES for wings, and on a hybrid RANS/LES approach. First AFOSR International Conference on DNS/LES, Advances in DNS/LES, Greyden Press.

Stefano, G. D. & Vasilyev, O. V. 2002 Sharp cutoff versus smooth filtering in large eddy simulation. *Phys. Fluids* **14**, 362–369.

Tammerman, L., Leschziner, M. A., Mellen, C. P. & Fröhlich, J. 2003 Investigation of wall-function approximations and subgrid-scale models in large eddy simulation of separated flow in a channel with streamwise periodic constrictions. *Int. J. Heat Fluid Flow.* **24**, 157–180.

Tannehill, J., Anderson, D. & Pletcher, R. 1997 *Computational fluid mechanics and heat transfer*. Taylor & Francis.

Tawfek, A. A. 1996 Heat transfer and pressure distributions of an impinging jet on a flat surface. *Heat Mass Transf.* **32**, 49–54.

Thomas, F. O. & Chu, H. C. 1989 An experimental investigation of the transition of a planar jet: Subharmonic suppression and upstream feedback. *Phys. Fluids A* **1**, 1566–1587.

Thomas, F. O. & Goldschmidt, V. W. 1985 The possibility of a resonance mechanism in the developing two-dimensional jet. *Phys. Fluids* **28**, 3510–3514.

Tritton, D. J. 1988 *Physical fluid dynamics*. Oxford Science Publ.

Tso, J. & Hussain, F. 1989 Organized motions in a fully developed turbulent axisymmetric jet. *J. Fluid Mech.* **203**, 425–448.

Tsubokura, M., Kobayashi, T., Taniguchi, N. & Jones, W. P. 2003 A numerical study on the eddy structures of impinging jets excited at the inlet. *Int. J. Heat Fluid Flow* **24**, 500–511.

Tu, C. V. & Wood, D. H. 1996 Wall pressure and shear stress measurements beneath an impinging jet. *Exp. Thermal Fluid Sci.* **13**, 364–373.

Umeda, Y., Maeda, H. & Ishii, R. 1987 Discrete tones generated by the impingement of a high-speed jet on a circular cylinder. *Phys. Fluids* **30**, 2380–2388.

Vasilyev, O. V., Lund, T. S. & Moin, P. 1998 A general class of commutative filters for LES in complex geometries. *J. Comp. Phys.* **146**, 82–104.

Viskanta, R. 1993 Heat transfer to impinging isothermal gas and flame jets. *Exp. Thermal Fluid Sci.* **6**, 111–134.

Wang, M. 1999 LES with wall models for trailing-edge aeroacoustics. *Annual Research Briefs,* pp. 355–364. Center for Turbulence Research, NASA Ames-Stanford University.

Wen, M.-Y. & Jang, K.-J. 2003 An impingement cooling on a flat surface by using circular jet with longitudinal swirling strips. *Int. J. Heat Mass Transf.* **46**, 4657–4667.

Yapici, S., Kuslu, S., Ozmetin, C., Ersahan, H. & Pekdemir, T. 1999 Surface shear stress for a submerged jet impingement using electrochemical technique. *J. Appl. Electrochemistry* **29**, 185–190.

Yoda, M., Hesselink, L. & Mungal, M. G. 1992 The evolution and nature of large-scale structures in the turbulent jet. *Phys. Fluids A* **4**, 803–811.

Zaman, K. B. M. Q. & Hussain, A. K. M. F. 1981 Turbulence suppression in free shear flows by controlled excitation. *J. Fluid Mech.* **103**, 133–159.